Asynchronous Concurrent Wireless Power Transfer in Sustainable 6G Networks: A Systematic Analysis

Ye Liu, *Senior Member, IEEE,* Mikael Gidlund, *Fellow, IEEE,* Honggang Wang, *Fellow, IEEE,* and Shucheng Yu, *Fellow, IEEE*

***Abstract*—6G networks require a sustainable and dependable power supply to ubiquitous space–air–ground connectivity infrastructures. Wireless power transfer (WPT) offers a promising path to sustainable energy delivery; however, concurrent transmitters can experience destructive interference when operating asynchronously. Most existing studies focus on centralized or synchronized WPT systems, leaving the asynchronous regime largely unexplored. In contrast to 5G's tightly coordinated and slowly varying links, 6G WPT must function under non-stationary mobility, higher carrier frequencies, and dense power transmitter deployments. To bridge this gap, we translate key 6G stressors into design laws and probability guarantees. Specifically, we present a new systematic framework for asynchronous concurrent WPT, featuring a unified kernel that captures frequency, timing, and phase dispersions as a single retention term across instantaneous, short-time, and long-time scales. Further, we provide closed-form ppm/time budgets for a target retention, a retention cumulative distribution function that tightens as $O(N^{-2})$, and a Doppler time-to-null scheduler coupled to the harvester. Finally, we perform deterministic and Monte Carlo analyses, together with experimental studies.**

***Index Terms*—wireless power transfer, 6G networks, concurrent transmission, asynchronous wireless powering, design laws.**

I. Introduction

THE evolution toward sixth-generation (6G) networks [1] is expected to expand connectivity across healthcare, agriculture, industrial automation, smart cities, and other sensing-intensive domains. These systems will rely on ultra-dense deployments, AI-assisted control, and heterogeneous devices ranging from microwatt-scale sensors to high-power radios. A central challenge is therefore sustainable and dependable power provisioning at scale, especially for mobile and aerial nodes with limited onboard energy [2].

Solar energy is widely used for sustainable operation [3], but it is inherently intermittent because of diurnal cycles, weather, shading, and geographic constraints [4]. Dependence on terrestrial refueling or charging infrastructure also introduces logistics and cost, especially for remote or high-altitude platforms [5]. Far-field radio frequency wireless power transfer (WPT) [6]–[8] therefore provides a complementary path by wirelessly delivering energy to devices, extending runtime, reducing battery replacement, and enabling low-maintenance operation, as illustrated in Fig. 1.

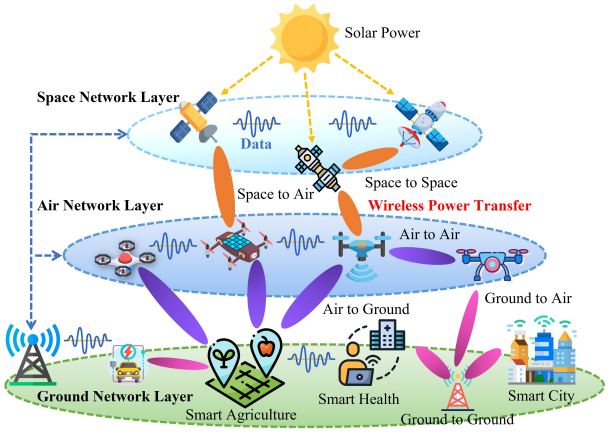

Fig. 1. WPT for sustainable 6G networks from space to ground.

To enlarge coverage and support diverse loads, wireless power transmitters are often activated concurrently [9]–[11]. While this improves coverage, spatial diversity, and load sharing, it also introduces energy interference [12]: when multiple waves superimpose at the receiver, imperfect coherence can produce constructive or destructive combining [13], [14]. In practice, the dominant cause is asynchronicity among distributed transmitters, including frequency offsets [15], time offsets [16], and phase offsets [17].

These impairments are not unique to 6G, but they can become more pronounced in emerging 6G WPT scenarios because of non-stationary mobility (e.g., UAVs, robots, and users), higher carrier frequencies, and larger transmitter ensembles. Under such conditions, a single average received-power number can be misleading because coherence loss depends strongly on the observation timescale and offset statistics. However, most existing studies focus either on centrally controlled power-beaming arrays [18] or on distributed concurrent WPT under synchronous/additive assumptions [19]. Recent distributed beamforming approaches attempt phase alignment [17], but are typically evaluated in small-scale settings with idealized feedback. Systematic multi-timescale analysis and actionable design guidelines for asynchronous concurrent WPT remain limited.

To bridge this gap, this paper develops a unified framework

Ye Liu is with the Department of Graduate Computer Science and Engineering, Katz School of Science and Health, Yeshiva University, New York, NY 10016 USA and the Department of Computer and Electrical Engineering, Mid Sweden University, 85170 Sundsvall, Sweden (e-mail: ye.liu@miun.se).

Mikael Gidlund is with the Department of Computer and Electrical Engineering, Mid Sweden University, 85170 Sundsvall, Sweden (e-mail: mikael.gidlund@miun.se).

Honggang Wang (corresponding author) and Shucheng Yu are with the Department of Graduate Computer Science and Engineering, Katz School of Science and Health, Yeshiva University, New York, NY 10016 USA (e-mail: honggang.wang@yu.edu, shucheng.yu@yu.edu).

for asynchronous concurrent WPT in realistic 6G settings. We systematically quantify how frequency, timing, and phase offsets affect harvested-energy behavior across timescales through the design-law mapping $\{\Delta f, \Delta\tau, \Delta\phi\} \xrightarrow{\Gamma(T_s)} \{P_{\text{inst}}(t), P_{\text{short}}(T_s), P_{\text{long}}\}$, where $\Gamma(T_s)$ is a unifying kernel that captures partial coherence over the harvester's effective averaging window T_s. Building on this formulation, we conduct deterministic and statistical analyses and experimentally illustrate key asynchronous effects using a commercial Powercast wireless power testbed. The resulting framework yields practical offset budgets and design guidelines for dependable multi-transmitter wireless charging without heavy infrastructure or tight synchronization. Specifically, the contributions of this paper are as follows:

- To the best of our knowledge, this is the first systematic multi-timescale framework for asynchronous concurrent WPT in space–air–ground integrated sustainable 6G networks. It provides closed-form trends and design laws that map into network-level decisions.
- We propose a pairwise coherence kernel that unifies frequency, timing, and phase dispersion into a single retention term over the harvester's effective window. This model supports deterministic analysis, Monte Carlo studies, and experimental illustration.
- We translate mobility-induced frequency offsets into Doppler-aware media access control (MAC) design quantities, which support peak-capture bursts, re-phasing cadence, and stable observation windows.
- We characterize retention cumulative distribution functions (CDF) under ppm spread, timing jitter, and phase variability across carrier frequency, transmitter count, and averaging window, thereby providing probabilistic guarantees beyond single average values.
- We derive closed-form offset budgets for distributed asynchronous WPT, translating performance targets into tolerances on frequency drift, timing skew, and phase spread, with additive budgeting rules across transmitters.

The remainder of the paper is organized as follows. Sec. II reviews related work, and Sec. III presents the system model. Sec. IV develops the deterministic analysis, Sec. V gives statistical results and scaling laws, and Sec. VI reports experimental results. Finally, Sec. VII concludes the paper.

II. Related Work

1) Centrally Controlled Antenna-Array Power Beaming: Centrally controlled power beamforming drives co-located, tightly networked antenna arrays so that emitted waves add coherently at intended receivers. The underlying principle is classical phased-array beamforming: track propagation phases and program per-element phases for constructive far-field combining. This line includes microwave WPT testbeds and coordinated array designs for energy focusing [18], [20]–[23]. Related surveys also summarize passive and active multibeam phased-array architectures for simultaneous multi-node powering [24]. These approaches, however, typically rely on substantial infrastructure, including tight synchronization, calibration, reliable control/fronthaul, accurate localization or channel state information (CSI), and continuous feedback to maintain coherence. By contrast, our work targets distributed WPT networks in which transmitters operate independently or only loosely coordinated. We therefore focus on models and design principles that remain effective under partial information, limited coordination, and intrinsic asynchronicity.

2) Synchronous Concurrent WPT in Distributed Networks: Concurrent WPT in distributed networks is commonly modeled in two ways: (i) the additive power model [25], [26], which sums per-transmitter received powers, and (ii) the ideal synchronous model [10], [27], which accounts for wave superposition under perfect phase alignment. These abstractions support a broad literature on charger placement, sensor placement, and charging scheduling [19]. However, each model has clear scope limits. The additive model is appropriate for long-term average power, but it obscures short-time variability. The ideal synchronous model captures spatial interference but assumes perfect synchrony and thus overlooks temporal coherence mechanisms that dominate in practice. Our work moves beyond both abstractions by developing a multi-timescale framework that explicitly models frequency, time, and phase offsets and their dispersions, enabling principled guidance for loosely coordinated distributed WPT networks [28].

3) Practical Asynchronous Concurrent WPT: Empirical studies [12] show that concurrent WPT can exhibit substantial temporal variation when transmitters do not share a common reference. Small but persistent frequency offsets, phase drift, and time skew can turn constructive combining into partial or deep cancellation over time. In parallel, recent feedback-based distributed beamforming methods [17], [29] show that frequency/phase misalignment can be iteratively corrected, but they generally rely on reliable feedback, tight coordination loops, and nontrivial orchestration overhead. In contrast, we treat asynchronicity as the default regime for distributed WPT. We develop a systematic quantitative framework that characterizes power retention under frequency, time, and phase dispersions, and show how dependable multi-transmitter charging can still be achieved with minimal infrastructure and control.

III. System Modeling

A. Root Causes of Asynchronicity

The dominant causes can be grouped into three coupled offset dimensions. Frequency offset arises from oscillator mismatch, hardware drift, aging, and mobility-induced Doppler effects. Time offset refers to temporal misalignment among concurrent waveforms. It may result from software scheduling delay, lack of global synchronization, propagation-delay differences, or heterogeneous control loops across static, mobile, and aerial platforms. Phase offset denotes the instantaneous angular mismatch among transmit signals. It is caused by oscillator startup differences, propagation-induced phase shifts, hardware inconsistency, and phase drift accumulated from frequency mismatch. These three impairments are not necessarily independent in practice, but together they determine the coherence level of concurrent WPT. Therefore, the following model characterizes asynchronous concurrent WPT through frequency, time, and phase dispersions and studies their impact across instantaneous, short-time, and long-time power scales.

B. Offset Model

a) Frequency Offset: Each transmitter j deviates from the nominal carrier f_t:

$$f_j(t) = f_t + \delta f_j + f_{D,j}(t), \tag{1}$$

where δf_j is the static frequency offset (e.g., ppm-level drift), and $f_{D,j}(t)$ is Doppler due to motion or geometry changes.

b) Time Offset: Without tight central coordination, emissions start at different times. Let the global reference time be $\tau_0 = 0$ and denote the start delay of node j as $\Delta\tau_j$.

c) Phase Offset: The received carrier phase of node j is

$$\theta_j(t) = \phi_j^{\text{init}} - \frac{2\pi d_j(t)}{\lambda} + \epsilon_j, \tag{2}$$

with initial phase ϕ_j^{init}, distance $d_j(t)$, wavelength λ, and hardware error ϵ_j. The pairwise phase difference is

$$\Delta\theta_{ij}(t) = \big(\phi_i^{\text{init}} - \phi_j^{\text{init}}\big) - \frac{2\pi}{\lambda}\big(d_i(t) - d_j(t)\big) + (\epsilon_i - \epsilon_j). \tag{3}$$

C. Composite Signal Model

1) Transmitter Geometry: Let N wireless power transmitters be located at $\mathbf{r}_j(t) = (x_j, y_j, z_j)$, and the receiver at $\mathbf{r}_0(t) = (x_0, y_0, z_0)$. The Euclidean distance is:

$$d_j(t) = \|\mathbf{r}_j(t) - \mathbf{r}_0(t)\|. \tag{4}$$

2) Amplitude Modeling: The received voltage-like amplitude from transmitter j is modeled via the Friis equation:

$$A_j(t) = \sqrt{P_{tj} G_{tj} G_r} \cdot \frac{\lambda}{4\pi d_j(t)} \cdot h_j(t), \tag{5}$$

where P_{tj} is the transmit power, G_{tj} and G_r are antenna gains, $h_j(t)$ captures fading. We use $h_j(t) = 1$ for LoS-dominant simplification; Rayleigh/Rician baselines given in Sec. III-E2.

3) Received Signal with Asynchronous Impairments: Combining above, the full instantaneous phase of transmitter j is:

$$\psi_j(t) = 2\pi \int_0^{t-\Delta\tau_j} f_j(\tau)\, d\tau + \theta_j(t - \Delta\tau_j). \tag{6}$$

The received electric field is:

$$E_j(t) = A_j(t - \Delta\tau_j) \cos\big(\psi_j(t)\big). \tag{7}$$

4) Superposed Signal: The total received electric field is the sum of all contributions:

$$E_{\text{total}}(t) = \sum_{j=1}^{N} E_j(t). \tag{8}$$

D. Multi-Perspective Power Model

Because asynchronous concurrent WPT is shaped by frequency, time, and phase offsets, the received power becomes inherently time-varying. A single scalar power value is therefore inadequate for practical characterization. We instead use a multi-perspective power model that captures behavior over three complementary timescales:

1) **Instantaneous Power:** Captures the fine-grained, sub-microsecond variations due to carrier-level constructive and destructive interference.
2) **Short-Time Average Power:** Represents the energy effectively accumulated over the charging time constant of practical RF-to-DC conversion circuits.
3) **Long-Time Expected Power:** Describes the statistical mean over extended periods, serving as a baseline for capacity planning and performance bounds.

a) Instantaneous Power: Using the composite signal model in Eq. (7), the instantaneous RF power is:

$$P_{\text{inst}}(t) = \left[\sum_{j=1}^{N} A_j(t - \Delta\tau_j) \cos\big(\psi_j(t)\big)\right]^2. \tag{9}$$

b) Short-Time Average Power: Most energy harvesting circuits integrate input RF power over a non-zero interval due to the finite charging time constant of rectifiers or storage elements. To reflect this behavior, we define:

$$P_{\text{short}}(t) = \frac{1}{T_s} \int_t^{t+T_s} P_{\text{inst}}(\tau)\, d\tau, \tag{10}$$

where T_s is the time window. For closed-form transparency, we use a rectangular average on $[0, T_s]$. For hardware-driven design, we set $T_s = T_{\text{rectifier}}$ and adopt the exponential envelope. Analysis compares like-for-like equivalent noise bandwidth, so the trends and budgets are unchanged; only constants differ slightly. $P_{\text{short}}(t)$ smooths out carrier-level fluctuations and provides a direct link to whether the accumulated energy in a given time slot exceeds the minimum threshold for a device operation. This perspective is important for identifying intermittent harvesting, predicting outages/brownouts, and supporting energy-aware MAC and task scheduling based on smoothed energy availability.

c) Long-Time Expected Power: For high-level network planning and statistical performance guarantees, we define:

$$P_{\text{long}} = \lim_{T\to\infty} \frac{1}{T} \int_0^T P_{\text{inst}}(t)\, dt, \tag{11}$$

Under the assumptions that $\phi_j^{\text{init}} \sim \mathcal{U}(0, 2\pi)$ i.i.d., δf_j and $\Delta\tau_j$ are static or slowly varying, and there is no active synchronization among transmitters, the cross terms in Eq. (9) vanish in expectation, yielding:

$$P_{\text{long}} = \frac{1}{2} \sum_{j=1}^{N} A_j^2(t - \Delta\tau_j). \tag{12}$$

This incoherent summation provides a robust lower bound under worst-case asynchronous conditions. It supports capacity planning to determine the number and power levels of transmitters needed to meet device energy demand; stochastic control to design duty cycles and wake-up schedules around statistical energy guarantees; and performance benchmarking to quantify the gain from partial or full synchronization strategies by comparing against this baseline. It should be noted that P_{long} characterizes the RF-domain incoherent limit under phase decorrelation. Due to the nonlinear transfer characteristic of RF–DC conversion, however, the corresponding average harvested DC power may still depend on higher-order envelope statistics, such as fluctuation variance, even when the long-term mean RF power is unchanged.

E. Practical Considerations

To translate our model into actionable 6G design rules, we further consider the following practical aspects.

1) Unifying Kernel $\Gamma(T_s)$ and Power Retention: In asynchronous concurrent WPT, misalignments arise from multiple sources and their impact depends on the harvester timescale T_s. Treating each impairment separately leads to case-by-case formulas that are hard to compare across f_c, N, mobility, or hardware memory. We therefore adopt a pairwise coherence kernel $|\Gamma_{ij}(T_s)| \in [0,1]$ that factorizes these dispersions into a single retention term. More generally, the pairwise kernel can be viewed as the magnitude of the averaged complex phasor under an aggregate short-time phase perturbation, i.e.,

$$\Gamma_{ij}(T_s) = \left|\mathbb{E}\big[\exp\big(j\,\Delta\Psi_{ij}(T_s)\big)\big]\right|, \tag{13}$$

where $\Delta\Psi_{ij}(T_s)$ denotes the effective pairwise phase perturbation induced by phase, timing, and frequency offsets over the averaging window T_s.

The factorized form adopted below is used as a tractable and physically interpretable approximation under a separable kernel construction, in which phase, timing, and frequency offsets contribute distinct pairwise coherence losses over the short-time interaction window. Specifically, the phase term captures random phasor misalignment, the timing term captures coherence loss induced by temporal slip relative to the carrier-scale structure, and the frequency term captures coherence attenuation accumulated over the averaging window T_s. Under this modeling assumption, the overall pairwise retention is written as the product of the corresponding phase, time, and frequency retention factors. Correlation among these offsets would introduce cross terms in a more general joint formulation; however, the separable form below provides the baseline design law used in this paper. For each pair (i,j) and averaging window T_s, the unified coherence kernel is

$$\Gamma_{ij}(T_s) = \underbrace{e^{-\sigma_{\theta,ij}^2/2}}_{\text{phase}} \cdot \underbrace{e^{-(2\pi f_c)^2\,\sigma_{\tau,ij}^2/2}}_{\text{time}} \cdot \underbrace{\Phi_f\big(\sigma_{f,ij}, T_s\big)}_{\text{frequency}}, \tag{14}$$

where $\sigma_{\theta,ij}$, $\sigma_{\tau,ij}$, and $\sigma_{f,ij}$ are the pairwise standard deviations of phase offset, time slip, and instantaneous frequency offset over the window T_s.

The timing-dispersion term is used under a Gaussian small-to-moderate jitter assumption, which is appropriate when the effective timing fluctuation is not excessively large relative to the carrier-scale structure. For large, strongly bounded, or substantially non-Gaussian timing jitter, the same general kernel framework remains applicable, but the timing factor should be replaced by the corresponding expression induced by the actual jitter distribution. In addition, the Gaussian modeling of time and phase offsets is adopted here as a tractable effective-statistics baseline for design-law extraction. This choice captures the dominant influence of second-order dispersion in a compact closed form, while the same general kernel framework can accommodate non-Gaussian offset statistics through the corresponding characteristic-function-based expressions when needed.

We use two standard frequency models, depending on the behavior of the pairwise frequency offset within the averaging window T_s.

(A) Quasi-static offset over T_s [30]: when the pairwise frequency offset remains approximately constant within the averaging window, i.e., $\Delta f_{ij}(t) \approx \Delta f_{ij}$ for $t \in [0, T_s]$, the frequency retention factor is

$$\Phi_f(\Delta f_{ij}, T_s) = \mathrm{sinc}(\pi\,\Delta f_{ij}\,T_s). \tag{15}$$

(B) Within-window wander [31]: when the instantaneous pairwise frequency offset exhibits non-negligible random fluctuation within T_s, modeled by a zero-mean Gaussian variable with standard deviation $\sigma_{f,ij}$, the frequency retention factor becomes

$$\Phi_f(\sigma_{f,ij}, T_s) = \frac{\sqrt{\pi}\,\mathrm{erf}\big(\sqrt{2}\pi\,\sigma_{f,ij}T_s\big)}{2\sqrt{2}\pi\,\sigma_{f,ij}\,T_s}. \tag{16}$$

With equal-amplitude normalization, the short-time RF power retention (PR) at window T_s is

$$\mathrm{PR}(T_s) = \frac{1}{N} + \Big(1 - \frac{1}{N}\Big)\bar{\Gamma}(T_s), \tag{17}$$

$$\bar{\Gamma}(T_s) = \frac{2}{N(N-1)} \sum_{i<j} \Gamma_{ij}(T_s). \tag{18}$$

They are presented under equal-amplitude normalization, which is adopted here as a baseline setting to isolate the impact of asynchronous phase, timing, and frequency offsets from geometry and path-loss induced amplitude imbalance. Under this normalization, the resulting retention law admits a compact closed form and highlights the coherence-loss mechanism most transparently. More generally, the equal-amplitude normalization can be relaxed by allowing unequal effective received amplitudes $\{a_i\}_{i=1}^N$, which may arise from distance-dependent path loss, blockage, antenna-pattern differences, or hardware mismatch. In that case, the normalized short-time RF power retention takes the weighted form

$$\mathrm{PR}_{\mathrm{w}}(T_s) = \frac{\sum_{i=1}^N a_i^2 + 2\sum_{i<j} a_i a_j\,\Gamma_{ij}(T_s)}{\Big(\sum_{i=1}^N a_i\Big)^2}, \tag{19}$$

where $\Gamma_{ij}(T_s)$ is the pairwise coherence kernel defined in Eq. (14). By defining the normalized amplitude weights

$$w_i \triangleq \frac{a_i}{\sum_{k=1}^N a_k}, \qquad \sum_{i=1}^N w_i = 1, \tag{20}$$

Eq. (19) can be rewritten as

$$\mathrm{PR}_{\mathrm{w}}(T_s) = \sum_{i=1}^N w_i^2 + 2\sum_{i<j} w_i w_j\,\Gamma_{ij}(T_s). \tag{21}$$

Introducing the weighted pairwise average kernel

$$\bar{\Gamma}_{\mathrm{w}}(T_s) \triangleq \frac{\sum_{i<j} w_i w_j\,\Gamma_{ij}(T_s)}{\sum_{i<j} w_i w_j}, \tag{22}$$

the weighted retention can be expressed compactly as

$$\mathrm{PR}_{\mathrm{w}}(T_s) = \sum_{i=1}^N w_i^2 + \left(1 - \sum_{i=1}^N w_i^2\right)\bar{\Gamma}_{\mathrm{w}}(T_s). \tag{23}$$

Therefore, the equal-amplitude result in Eq. (18) is recovered as the special case $a_i \equiv a$, equivalently $w_i = 1/N$, for which $\bar{\Gamma}_{\mathrm{w}}(T_s) = \bar{\Gamma}(T_s)$. Accordingly, the equal-amplitude model should be interpreted as a tractable baseline for the balanced regime, while amplitude inconsistency is incorporated through the weighted pairwise form above. Under this weighted extension, the pairwise kernel structure and the retention aggregation law generalize directly to unequal amplitudes, whereas the compact closed-form expressions derived under equal-amplitude normalization should be interpreted as balanced-regime baseline results.

As $T_s \to 0$, both frequency models satisfy $\Phi_f \to 1$, meaning that frequency dispersion is not yet accumulated over an infinitesimal averaging window. Therefore,

$$\Gamma_{ij}(T_s) \to e^{-\sigma^2_{\theta,ij}/2}\, e^{-(2\pi f_c)^2\, \sigma^2_{\tau,ij}/2}, \tag{24}$$

corresponding to a quasi-coherent and peaky regime. As $T_s \to \infty$, the within-window wander model decays as $\Phi_f(\sigma_{f,ij}, T_s) \propto 1/(\sigma_{f,ij} T_s)$, which progressively washes out the cross terms and drives PR toward the incoherent limit. These behaviors make explicit how T_s trades peak capture for stability. In summary, Eq. (15) is selected when the pairwise frequency offset is effectively deterministic over the averaging window (e.g., static ppm mismatch or very slow drift relative to T_s), whereas Eq. (16) is selected when random within-window frequency wander is non-negligible (e.g., oscillator wander, phase-noise-induced fluctuation, or residual Doppler variation within T_s).

For a target retention $R_{\min}$ under i.i.d. ppm with std σ_{ppm} (so that $\sigma_{f,ij} \approx \sqrt{2}\, f_c\, \sigma_{\mathrm{ppm}} \times 10^{-6}$), a conservative small-dispersion bound is

$$\boxed{\sigma_{\mathrm{ppm}} \lesssim \frac{\sqrt{3\big(1-R_{\min}\big)}}{\pi f_c T_s \sqrt{1-1/N}} \cdot 10^6}, \quad \mathrm{Var}(\mathrm{PR}) = O\big(N^{-2}\big). \tag{25}$$

Lemma 1 (Retention guarantee (large-N and one-sided bound)). Let $X_{ij} = \Gamma_{ij}(T_s)$ with mean μ and variance σ^2. For equal amplitudes,

$$\mathrm{PR} = \frac{1}{N} + \Big(1 - \frac{1}{N}\Big)\, \bar{X}, \quad \bar{X} = \frac{1}{\binom{N}{2}} \sum_{i<j} X_{ij}. \tag{26}$$

For large N,

$$\Pr\{\mathrm{PR} > r\} \approx 1 - \Phi\left(\frac{r - \big[\frac{1}{N} + (1-\frac{1}{N})\mu\big]}{(1-\frac{1}{N})\, \sigma / \sqrt{\binom{N}{2}}} \right). \tag{27}$$

For any N, the one-sided Chebyshev (Cantelli) inequality gives

$$\Pr\{\mathrm{PR} \le r\} \le \frac{\mathrm{Var}(\mathrm{PR})}{\mathrm{Var}(\mathrm{PR}) + (\mathbb{E}[\mathrm{PR}] - r)^2}, \mathrm{Var}(\mathrm{PR}) = \big(1 - \tfrac{1}{N}\big)^2\, \frac{\sigma^2}{\binom{N}{2}} \tag{28}$$

This scaling highlights the core 6G levers: higher f_c or shorter T_s tighten ppm budgets, whereas larger N concentrates PR around its mean, reflecting the law of large numbers on the cross terms. More generally, under unequal amplitudes, the same interpretation carries over through Eq. (23), with $\sum_i w_i^2$ quantifying the self-term dominance and $\bar{\Gamma}_{\mathrm{w}}(T_s)$ capturing the amplitude-weighted pairwise coherence retention. It should be emphasized that the proposed ppm/time budgets are intended as RF-domain design guidelines for maintaining favorable coherence and retention conditions, rather than universal end-to-end guarantees of dependable charging. In practical hardware, the eventual DC-side outcome may still be modified by rectifier nonlinearities, storage dynamics, and MPPT/control interactions, especially at higher input power levels.

2) Channel Realism: Assuming $h_i(t) = 1$ may overstate coherence gains and raise stability concerns. In practice, large/small–scale effects set a baseline level, while asynchronous penalties still enter via the pairwise kernel $\Gamma_{ij}(T_s)$. Making this split explicit keeps the math simple and conclusions robust. Let the complex baseband channel for link i be

$$h_i(t) \;=\; \sqrt{\beta_i}\, g_i, \qquad g_i = \mu_i + w_i, \tag{29}$$

where β_i captures large–scale effects (path loss, shadowing, polarization/coupling folded into a_i if preferred), g_i is small–scale fading with LoS component μ_i and diffuse component $w_i \sim \mathcal{CN}(0, \sigma_w^2)$. The Rician factor is $K_i = |\mu_i|^2/\sigma_w^2$ (with $K_i \to \infty \Rightarrow$ LoS; $K_i = 0 \Rightarrow$ Rayleigh). We take $\{\beta_i\}$ independent of offsets and of $\{g_i\}$ over the window T_s.

With the unified kernel, the windowed short-time RF power can be written as a baseline plus coherent cross terms:

$$P_{\text{short}}(T_s) = \tfrac{1}{2} \sum_{j=1}^{N} a_j^2\, \beta_j + \sum_{i<j} a_i a_j\, \Re\Big\{ \sqrt{\beta_i \beta_j}\, g_i g_j^*\, \Gamma_{ij}(T_s) \Big\}. \tag{30}$$

If $K_i = 0$ for all i so that $\mathbb{E}[g_i] = 0$, the cross terms vanish in expectation and the baseline is

$$\text{Rayleigh floor: } \mathbb{E}[P_{\text{short}}(T_s)] = \tfrac{1}{2} \sum_{j=1}^{N} a_j^2\, \mathbb{E}[\beta_j]. \tag{31}$$

If $K_i > 0$, $\mathbb{E}[g_i] = \mu_i$ and the mean retained cross term is

$$\text{Rician pedestal: } \mathbb{E}\Big[\Re\Big\{ \sqrt{\beta_i \beta_j}\, g_i g_j^* \Big\}\Big] = \sqrt{\mathbb{E}[\beta_i]\, \mathbb{E}[\beta_j]}\; \Re\{\mu_i \mu_j^*\}. \tag{32}$$

These equations show that fading adjusts only the baseline (Rayleigh floor) and the LoS pedestal. All asynchrony penalties and timescale effects still enter via the same $\Gamma_{ij}(T_s)$. Thus: (i) keeping $h_i = 1$ is a LoS-dominant simplification; (ii) finite-K and Rayleigh regimes reduce the mean and increase variance but do not alter the unified kernel mechanics; (iii) antenna placement, polarization, and blockage act through a_i and β_i, while MAC/harvester timing acts through T_s.

3) Doppler as a MAC-Level Timer: Without a timing rule, offset analyses risk being descriptive but not prescriptive. Doppler directly sets how long quasi-coherence lasts while nodes move, so we convert it into a timer that drives burst length, re-phasing cadence, and the choice of the observation/harvester window T_s. For any transmitter pair (i, j), $\Delta f_{ij}(t) = \big(\delta f_i - \delta f_j\big) + \big(f_{D,i}(t) - f_{D,j}(t)\big)$, and $\Delta\tau_{ij} = \Delta\tau_i - \Delta\tau_j$. The initial phase mismatch includes the time-offset contribution $\phi_{ij,0} = \phi_i - \phi_j + 2\pi f_t\, \Delta\tau_{ij}$. Over an interval where $\Delta f_{ij}(t)$ is approximately constant, the

dominant beat has period $T_{\text{beat}}^{(i,j)} \approx \frac{1}{|\Delta f_{ij}|}$. Starting from phase $\phi_{ij,0}$, the next destructive superposition (null) arrives at

$$t_{\text{null}}^{(i,j)} \approx \frac{\pi - \phi_{ij,0}}{2\pi\,|\Delta f_{ij}|}. \tag{33}$$

This is obtained under a local constant-Δf assumption, and is therefore intended as a short-interval beating approximation. It is accurate when the pairwise frequency offset varies slowly over the beating interval of interest. For moving-platform scenarios with non-negligible $d\Delta f/dt$, the predicted t_{null} should be interpreted as a local approximation; more generally, the null condition is governed by the accumulated relative phase under time-varying frequency offset. Likewise, for nonstationary or non-Gaussian Doppler processes, the same unified framework may still be applied at the level of effective short-time statistics, while the simple constant-Δf null law is no longer globally exact. Moreover, the assumption that fading is negligible within T_s is used at the short-time analysis level, where the channel is treated as approximately stationary over a locally frozen window. Mobility-induced Doppler and larger-scale channel evolution are instead understood as acting over longer time scales, and are captured through effective parameters that vary across successive windows rather than within a single short-time retention interval.

To make this rule robust without tracking every pair, select a percentile f_α of $|\Delta f_{ij}|$ (e.g., median or 90th) and define a guard time

$$t_g \;=\; \eta\,\frac{\pi - \phi_{ij,0}}{2\pi\, f_\alpha}, \qquad 0 < \eta < 1. \tag{34}$$

When $\phi_{ij,0}$ is unknown, a conservative choice is $\phi_{ij,0} = \frac{\pi}{2}$, giving $t_g = \eta/(4f_\alpha)$. As demonstrated in Fig. 2, it follows that in peak-capture mode, charge bursts of length $T_{\text{burst}} \le t_g$ and/or re-phasing every $T_r \le t_g$ should be scheduled to exploit quasi-coherent intervals where $\Gamma_{ij}(T_{\text{burst}})$ remains high. In stability mode, the observation/harvester window is set to $T_s \gg 1/f_\alpha$, ensuring that $\Gamma_{ij}(T_s) \approx 0$ and the received power converges to its incoherent baseline with low variance. In a hybrid policy, short peak-seeking bursts ($T_{\text{burst}} \le t_g$) are alternated with long stabilization windows ($T_s \gg 1/f_\alpha$), adapting to the battery state or quality-of-power requirements.

4) Tie the Math to the Harvester: Guarantees on RF retention are only actionable if they translate to load-side power. The rectifier-plus-storage front-end introduces memory and weak nonlinearity. Therefore, the averaging window used in the RF-side retention analysis should be matched to the timescale physically implemented by the harvester. Let $s(t) \triangleq E_{\text{total}}(t)$ denote the total received field. We model the harvester memory by the exponential kernel

$$\bar{w}_{T_s}(t) = \frac{1}{\tau_{RC}} e^{-t/\tau_{RC}} \mathbf{1}_{t\ge 0}, \tag{35}$$

where τ_{RC} is the effective RC time constant of the rectifier-plus-storage network, and $\mathbf{1}_{t\ge 0}$ is the indicator function. The corresponding smoothed envelope at the harvester input is $v(t) = \big|\,(s * \bar{w}_{T_s})(t)\,\big|$. Since the rectifier-plus-storage front-end behaves as a first-order envelope smoother, its memory can be approximated by the exponential kernel in (35). Therefore, we choose the averaging window as $T_s \triangleq T_{\text{rectifier}} \approx \tau_{RC}$, where

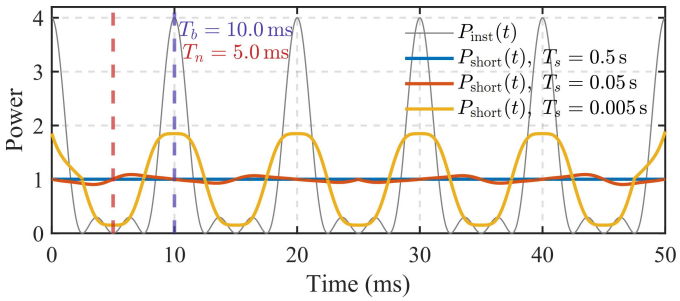

Fig. 2. Short-term power $P_{\text{short}}(t)$ for two unsynchronized Txs with $|\Delta f| = 100$ Hz ($T_{\text{beat}} = 1/|\Delta f|$). Vertical markers show T_{beat} and the first null T_n predicted by Eq. (33). MAC guidance: set burst length T_{burst} and re-phasing interval T_r at or below the guard time $t_g = \eta T_n$ from Eq. (34) to exploit quasi-coherent peaks. For stability, choose the averaging window $T_s \gg T_{\text{beat}}$ so P_{short} approaches the incoherent baseline.

$T_{\text{rectifier}}$ denotes the effective rectifier response timescale, i.e., the characteristic time over which the rectifier/output stage responds to RF-envelope variations. Accordingly, T_s is not introduced as an abstract signal-processing window, but as the effective harvester-memory timescale determined by the rectifier-plus-storage front-end.

This choice is physically motivated by timescale matching: T_s should be much larger than the carrier period so that carrier-scale oscillations are averaged out, while remaining on the order of the harvester memory timescale so that envelope variations relevant to rectification and energy accumulation are still retained. In this way, the averaging window used in the PR definition is aligned with the smoothing window physically implemented by the harvester front-end, making PR directly interpretable as a predictor of the smoothed envelope and, consequently, of load-side harvested power.

This exponential kernel approximates the rectifier+storage RC memory. Using it here and in PR eliminates averaging artifacts. Second-order modeling suffices at low power. For weak nonlinearity, the fourth-order correction is included:

$$P_{\text{DC}} \;\approx\; c_2\,\mathbb{E}\big[v^2\big] \;+\; 3c_4\,\mathbb{E}\big[v^2\big]^2, \tag{36}$$

where $c_2, c_4 > 0$ depend on diode and load parameters. The windowed second moment maps to the framework via the kernel

$$\mathbb{E}\big[v^2\big] \;\propto\; \tfrac{1}{2}\sum_{j=1}^{N} a_j^2 \;+\; \sum_{i<j} a_i a_j\,\Gamma_{ij}(T_s), \tag{37}$$

so that P_{DC} is obtained by substituting (37) into (36) with $T_s = T_{\text{rectifier}}$. Hence, in the square-law regime at very low input, $P_{\text{DC}} \propto \mathbb{E}[v^2]$, so constructive peaks from concurrency help proportionally, governed by $\Gamma_{ij}(T_s)$. In the weakly nonlinear regime, the $3c_4\mathbb{E}[v^2]^2$ term increases sensitivity to envelope variance and allows stronger beating or larger peaks to improve performance until storage or MPPT limits engage. In the saturation or MPPT-limited regime, once the rectifier or DC-DC stage saturates, additional cross-term retention no longer increases P_{DC}, so peak-seeking MAC strategies should back off to stability mode.

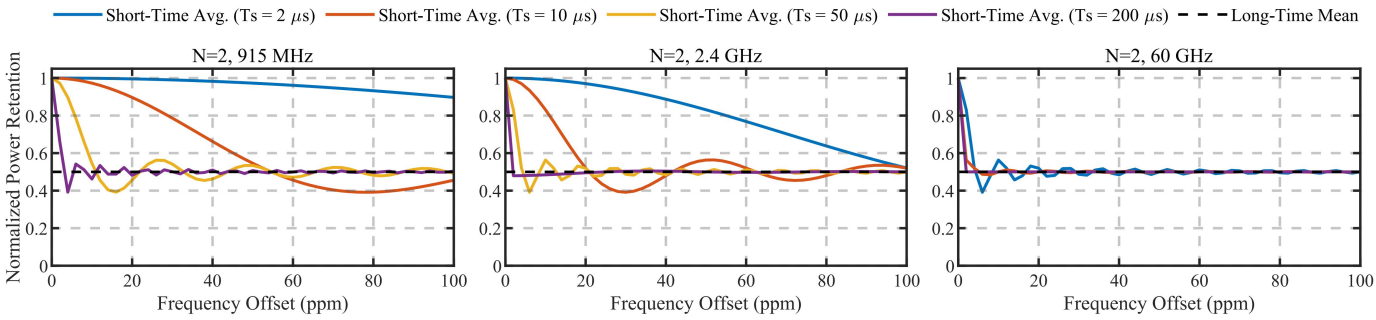

Fig. 3. Normalized power retention versus frequency offset for $N = 2$ at different carrier frequencies (915 MHz, 2.4 GHz, and 60 GHz). Each subplot shows the retention under various short-term averaging windows T_s (2, 10, 50, and 200 μs), compared against the long-time mean ($1/N = 0.5$). The results highlight how higher carrier frequencies lead to more rapid degradation of power retention under the same ppm frequency offset.

IV. Deterministic Analysis

This section develops a deterministic view of asynchronous concurrent WPT to reveal how phase, timing, and frequency offsets shape short-time coherence retention and power retention. We first focus on the two-transmitter case ($N = 2$), because it provides the clearest closed-form characterization of the underlying pairwise coherence-loss mechanism. This two-source case serves as the fundamental building block of the more general multi-transmitter setting. For $N > 2$, the same mechanism is incorporated through the pairwise kernels $\Gamma_{ij}(T_s)$ and their aggregation in power-retention expressions developed in the next section, which extend the deterministic insight from a single pair to the full transmitter ensemble.

A. Impact of Frequency Offset

1) Short-Time and Long-Time Average Power: As expected from the classic beating effect, with 0 ppm offset, the two carriers are perfectly synchronized and the instantaneous envelope power equals the coherent bound. Small offsets (e.g., 10 ppm) induce slow oscillations, while larger offsets (50–100 ppm) shorten the beat period and increase power fluctuations, illustrating that beat frequency scales with the frequency offset.

We now present short-time and long-time power analyses. Fig. 3 presents the normalized power retention versus frequency offset for the case of two concurrent transmitters ($N = 2$). Three carrier frequencies are considered: 915 MHz, 2.4 GHz, and 60 GHz. Several short-term averaging windows (T_s = 2–200 μs) are compared against the theoretical long-time mean value ($1/N = 0.5$).

At zero offset, the transmitters are fully coherent, resulting in maximum normalized retention equal to unity. As the frequency offset increases, retention decreases monotonically and approaches the long-time mean. The rate of this convergence depends strongly on the averaging interval. For short windows (e.g., $T_s = 2$ μs), the system still captures significant coherent gain because the beating cycles are not fully averaged. For longer windows, retention converges more rapidly to the theoretical asymptote, confirming the averaging effect of frequency mismatch. A comparison across carrier frequencies reveals that higher carrier frequencies are more vulnerable to ppm-level instabilities. For the same offset in parts-per-million, the absolute frequency deviation (Δf) is larger at 60 GHz than at 915 MHz. Consequently, retention decays faster at mmWave bands, emphasizing that frequency stability is particularly critical for high-frequency WPT deployments.

2) Takeaways: First, beating is the hallmark of frequency offset: any nonzero Δf produces envelope beating with period $T_b = 1/|\Delta f|$, where larger offsets shorten T_b and intensify the alternation between constructive and destructive interference. Second, short-time averaging T_s governs the retained coherence: when $T_s \ll T_b$, the system preserves significant coherent gain since beating is not fully averaged, whereas as T_s approaches or exceeds T_b, the short-time average converges rapidly to the long-time mean $1/N$. Third, carrier frequency further magnifies ppm errors, since for the same ppm, the absolute offset $\Delta f = \text{ppm} \times f_t$ is larger at higher f_t, leading to faster retention decay at 60 GHz than at 915 MHz and making frequency stability, or active correction, particularly critical at mmWave frequencies. Finally, from a design perspective, to maintain a target retention $\mathcal{R}_{\min}$ over a window T_s, one requires $T_b \gg T_s$ (equivalently $|\Delta f| \ll 1/T_s$), which yields a practical bound on allowable ppm drift $\text{ppm} \ll \frac{1}{f_t T_s}$.

B. Impact of Time Offset

1) Short-Time Retention and Long-Time Mean: From the classic phase misalignment perspective, we know that the instantaneous RF power depends on the relative delay. Squaring the RF sum produces a component at twice the carrier, giving two oscillations per RF period, with the mean envelope maximal at $\Delta\tau = 0$, minimal at $\Delta\tau = 0.5T$, and smoothly varying in between. With $\Delta f = 0$, no slow beating occurs over microseconds, leaving only the fast $2f_t$ ripple at the instantaneous timescale.

We next examine short-time and long-time power. Fig. 4 reports the normalized power retention versus time offset with the x-axis expressed as $\Delta\tau/T$. We overlay several short-time averaging windows $T_s \in \{2, 10, 50, 200\}$ μs using hollow markers to indicate each series. For $\Delta f = 0$, once T_s spans many carrier cycles the $2f_t$ ripple averages out and the retention follows the cosine law for two equal-amplitude tones, which is effectively independent of T_s. Consequently, all T_s curves coincide. The dashed horizontal reference at $1/N = 0.5$ shows the long-time mean baseline using incoherent sum.

2) Carrier Invariance: Unlike the frequency-offset case, the time-offset results are carrier-invariant once we normalize

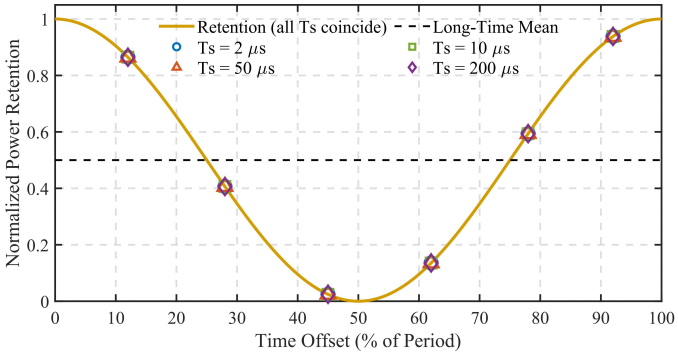

Fig. 4. Normalized power retention vs time offset ($\Delta\tau/T$) with hollow markers indicating $T_s \in \{2, 10, 50, 200\}\,\mu$s. For $\Delta f = 0$, all T_s series coincide with $R(\Delta\tau) = \frac{1+\cos(2\pi\,\Delta\tau/T)}{2}$; the dashed line shows the long-time mean $1/N = 0.5$.

by the carrier period. The retention depends only on the equivalent phase $\Delta\phi = 2\pi\,\Delta\tau/T$, so the curve $R(\Delta\tau/T)$ is identical at 915 MHz, 2.4 GHz, and 60 GHz. Plotting three separate subfigures would repeat the same cosine. Instead, we present a single, cleaner figure with hollow markers to denote different T_s. When absolute budgets are needed, one converts a given fractional offset to seconds via $|\Delta\tau| = (\Delta\tau/T)\,T$ (e.g., the same 15% of a period corresponds to ~ 0.164 ns at 915 MHz, ~ 0.062 ns at 2.4 GHz, and ~ 2.5 ps at 60 GHz).

3) Takeaways: First, a time offset is equivalent to a deterministic phase error $\Delta\phi = 2\pi\,\Delta\tau/T$, so it fixes the envelope level without inducing slow-time beating. Second, squaring the RF sum introduces a $2f_t$ component, hence $P_{\text{inst}}(t)$ shows two oscillations per RF period on the t/T axis while its mean level is set solely by $\Delta\tau/T$. Third, once the short-time window spans many carrier cycles, the $2f_t$ ripple averages out and the retention follows $R(\Delta\tau/T) = \frac{1+\cos(2\pi\,\Delta\tau/T)}{2}$, effectively independent of T_s. It is worth noting that this deterministic cosine-law time-offset result and the stochastic Gaussian timing-dispersion term describe different regimes. The former applies to a fixed delay offset in the deterministic two-source setting, whereas the latter applies when timing misalignment is modeled statistically through its effective jitter variance in the unified-kernel formulation. Fourth, normalizing by period makes the result carrier-invariant: the curve $R(\Delta\tau/T)$ is identical at 915 MHz, 2.4 GHz, and 60 GHz, so one plot suffices; absolute delay budgets follow from $|\Delta\tau| = (\Delta\tau/T)\,T$. Finally, a practical budget for two equal-amplitude transmitters to keep $\sim$1 dB loss ($R \gtrsim 0.8$) is $|\Delta\tau|/T \lesssim 0.15$, which corresponds to ~ 0.164 ns at 915 MHz, ~ 0.062 ns at 2.4 GHz, and ~ 2.5 ps at 60 GHz.

C. Impact of Phase Offset

Since a time offset at a single carrier is equivalent to a fixed phase error ($\Delta\phi = 2\pi\,\Delta\tau/T$), we have

$$\frac{\Delta\tau}{T} \;\longleftrightarrow\; \frac{\Delta\theta}{2\pi}, \qquad \text{with} \quad \Delta f = 0. \tag{38}$$

Below we highlight the aspects that differ operationally from time offset.

1) What is Different from Time Offset: Phase offset is naturally specified and calibrated in degrees/radians (via phase shifters or baseband phase control), whereas time offset is specified in ps/ns (via triggering, cable/air-path trimming). In addition, at a single tone, a fixed $\Delta\theta$ and a fixed $\Delta\tau$ are indistinguishable. To separate them one must probe at two or more frequencies (delay yields a linear phase slope vs. frequency, initial phase is flat). Moreover, phase noise (radians) and timing jitter (seconds) are different processes; mapping $\sigma_\theta = 2\pi f_t\,\sigma_\tau$ shows that the same timing jitter is more harmful at higher f_t, even though the static $R(\Delta\theta)$ curve itself is carrier-invariant. Finally, the pairwise $\cos(\Delta\theta_{ij})$ terms can create deep nulls for modest dispersion; simple phase alignment without retiming can recover most of the coherent gain in continuous wave settings.

2) Takeaways: First, the phase-offset results are algebraically identical to Section IV-B after replacing $\Delta\tau/T$ by $\Delta\theta/(2\pi)$; both set a fixed envelope level with no slow beating at $\Delta f = 0$. Second, for two equal amplitudes $R(\Delta\theta) = \frac{1+\cos\Delta\theta}{2}$ and is effectively independent of T_s once T_s spans many cycles. Third, a $\sim$1 dB budget ($R \gtrsim 0.794$) corresponds to $|\Delta\theta| \lesssim 0.941$ rad ($\approx 54^\circ$) and small-angle loss is quadratic, $R \approx 1 - \Delta\theta^2/4$. Finally, in practice phase control is often simpler than retiming for continuous waveform WPT; when absolute time budgets are needed, convert via $\Delta\tau = \Delta\theta/(2\pi f_t)$ to compare directly with Section IV-B.

V. Statistical Analysis

After showing deterministically how fixed offsets influence power behavior, this section turns to statistical analysis of performance under realistic uncertainty.

A. Impact of Frequency Offset

1) Monte Carlo Setup: We now quantify how random frequency error (ppm) degrades short-time coherent combining. As a baseline sensitivity model, each wireless power transmitter's normalized frequency error is modeled as i.i.d. Gaussian, $\varepsilon_i \sim \mathcal{N}(0, \sigma^2_{\text{ppm}})$. For carrier f_c, the pairwise offset is

$$\Delta f_{ij} = f_c \cdot 10^{-6}(\varepsilon_i - \varepsilon_j), \tag{39}$$

and the short-time pairwise coherence over an averaging window T_s is attenuated by $\operatorname{sinc}\big(\pi\,\Delta f_{ij} T_s\big)$.

The i.i.d. ppm assumption is adopted here as an idealized, decoupled baseline for tractable sensitivity analysis, rather than as a universally exact description of practical oscillator behavior. In real WPT hardware, especially at 2.4 GHz and more prominently at 60 GHz, frequency offsets may exhibit correlated drift due to common thermal conditions, shared environments, or coupled oscillator dynamics. Accordingly, the present Monte Carlo results should be interpreted as baseline frequency-sensitivity trends within the unified framework. For the 60 GHz case in particular, they are more appropriately viewed as qualitative high-frequency illustrations than as quantitatively complete oscillator-physics predictions.

We consider ppm errors to be quasi-static over the averaging window T_s because, for commodity crystal-oscillator

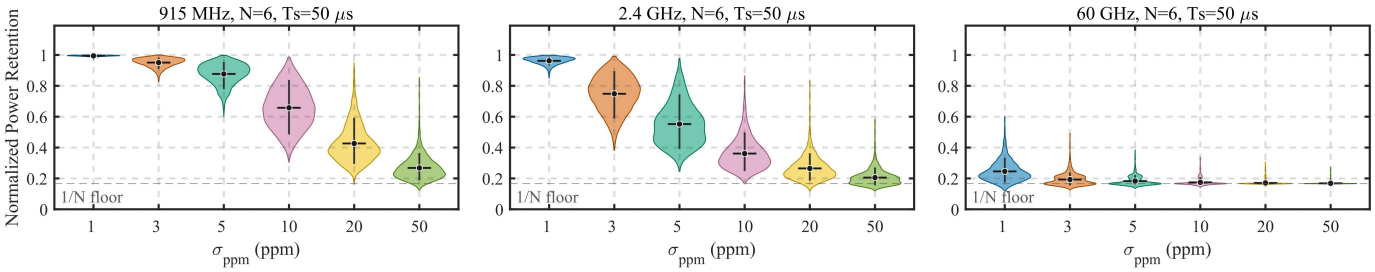

Fig. 5. Normalized power retention distributions versus Gaussian frequency error σ_{ppm} for $N = 6$ transmitters over an averaging window $T_s = 50$ μs. Subplots correspond to carriers (a) 915 MHz, (b) 2.4 GHz, and (c) 60 GHz. For each $\sigma_{\mathrm{ppm}} \in \{1, 3, 5, 10, 20, 50\}$ ppm, $M = 4000$ Monte Carlo trials draw i.i.d. ppm offsets per transmitter. Violins show empirical densities, with horizontal bars marking the means (dots overlaid) and vertical lines give 10–90% ranges. The dashed horizontal line indicates the incoherent $1/N$ floor.

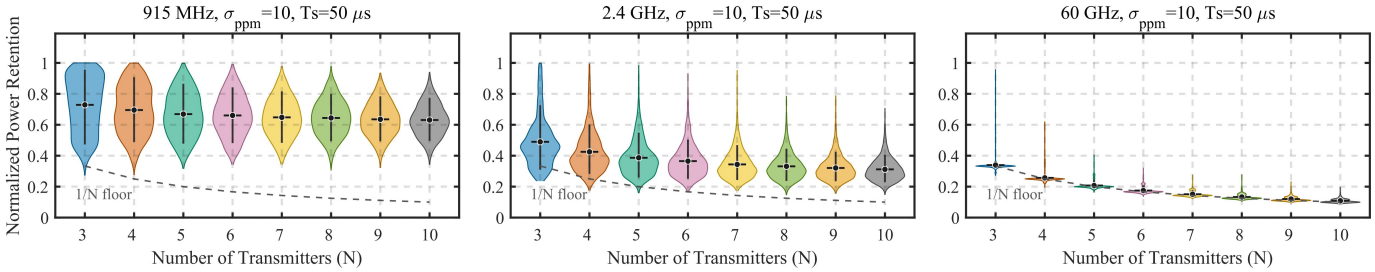

Fig. 6. Normalized power retention distributions versus the number of transmitters N under Gaussian frequency errors with fixed $\sigma_{\mathrm{ppm}} = 10$ and averaging window $T_s = 50$ μs. Subplots correspond to carriers (a) 915 MHz, (b) 2.4 GHz, and (c) 60 GHz. For each $N \in \{3, \ldots, 10\}$, $M = 4000$ Monte Carlo trials draw i.i.d. ppm offsets per transmitter. Violins show empirical densities, with horizontal bars marking the means (dots overlaid) and vertical lines indicate the 10–90% ranges. The dashed curve shows the incoherent $1/N$ floor.

references, the dominant frequency drift typically evolves on a much slower time scale than the short windows considered here. Thus, sub-10^2 ms windows fall within a locally "frozen" portion of the drift, and the intra-window wander is neglected relative to the mean ppm offset. Under this local constant-offset approximation, the pairwise short-time coherence equals

$$\Gamma_{ij}(T_s) = \mathrm{sinc}\big(\pi\, \Delta f_{ij} T_s\big). \tag{40}$$

In the unified kernel, this corresponds to

$$\sigma_{f,ij} = 0. \tag{41}$$

Thus, we summarize the frequency-induced coherence via

$$\kappa_f(T_s) = \frac{2}{N(N-1)} \sum_{i<j} \mathrm{sinc}\big(\pi\, \Delta f_{ij} T_s\big), \tag{42}$$

and

$$\mathrm{PR}(T_s) = \frac{1}{N} + \Big(1 - \frac{1}{N}\Big)\kappa_f(T_s), \tag{43}$$

where Power Retention (PR)$= 1$ is the coherent bound and $1/N$ is the normalized RF-power floor under equal-amplitude normalization in the incoherent limit. It should be noted that this floor is defined at the RF-domain retention level. Due to nonlinear RF–DC conversion, the corresponding harvested DC output need not scale identically. We estimate κ_f by Monte Carlo (4,000 trials per operating point) and display the full distribution of PR using violin plots (mean and 10–90% whiskers), rather than only an average.

2) PR vs ppm at 915 MHz / 2.4 GHz / 60 GHz: Fig. 5 shows PR distributions versus $\sigma_{\mathrm{ppm}} \in \{1, 3, 5, 10, 20, 50\}$ for $N = 6$ and $T_s = 50$ μs at $f_c \in \{915$ MHz, 2.4 GHz, 60 GHz$\}$. For a fixed ppm spread and window, higher carrier frequencies suffer larger absolute offsets ($|\Delta f| \propto f_c$), and thus earlier loss of coherence. At 915 MHz, tens of ppm remain serviceable. At 2.4 GHz, single-digit ppm already depresses PR. At 60 GHz, even a few ppm can push the distribution toward the $1/N$ baseline. The distribution width is largest in the partially coherent regime (neither near 1 nor near $1/N$), reflecting trial-to-trial sensitivity to unlucky offset constellations.

3) PR vs Number of Transmitters: Fig. 6 reports PR distributions versus $N \in \{3, \ldots, 10\}$ for $T_s = 50$ μs and $\sigma_{\mathrm{ppm}} = 10$ at the three carriers. We use $\sigma_{\mathrm{ppm}} = 10$ as a representative intermediate mismatch level, guided by the parameter sweep in Fig. 5, where $\sigma_{\mathrm{ppm}} \in \{1, 3, 5, 10, 20, 50\}$. Selecting this intermediate value helps illustrate the frequency-dispersion effect with a case that is neither too weak nor overly extreme. The dashed $1/N$ reference is overlaid. When frequency discipline is adequate (lower f_c or tighter ppm), increasing N yields visible gains above the $1/N$ floor. Conversely, when offsets dominate (e.g., 60 GHz at $\sigma_{\mathrm{ppm}} = 10$, $T_s = 50$ μs), the violins cluster near $1/N$, indicating that scaling N provides little benefit unless coherence is preserved.

4) PR vs Averaging Window: Fig. 7 shows PR versus $T_s \in \{2, 5, 10, 20, 50, 100, 200\}$ μs with $N = 6$ and $\sigma_{\mathrm{ppm}} = 10$. Increasing T_s averages more of the beat cycles caused by Δf_{ij}, driving $\kappa_f(T_s)$ downward and pushing PR toward $1/N$. The effect is most pronounced at 60 GHz and least at 915 MHz, consistent with the $|\Delta f| \propto f_c$ scaling.

This article has been accepted for publication in IEEE Journal on Selected Areas in Communications. This is the author's version which has not been fully edited and content may change prior to final publication. Citation information: DOI 10.1109/JSAC.2026.3699841

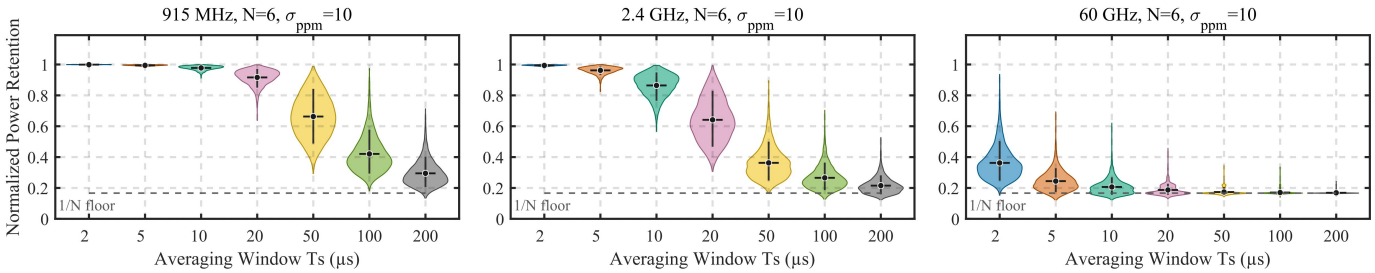

Fig. 7. Normalized power-retention distributions versus averaging window T_s for $N = 6$ transmitters under Gaussian frequency errors with fixed $\sigma_{\mathrm{ppm}} = 10$. Subplots correspond to carriers (a) 915 MHz, (b) 2.4 GHz, and (c) 60 GHz. For each $T_s \in \{2, 5, 10, 20, 50, 100, 200\}$ μs, $M = 4000$ Monte Carlo trials draw i.i.d. ppm offsets per transmitter. Violins show empirical densities, with horizontal bars marking the means (dots overlaid) and vertical lines indicate the 10–90% ranges. The dashed horizontal line shows the incoherent $1/N$ floor.

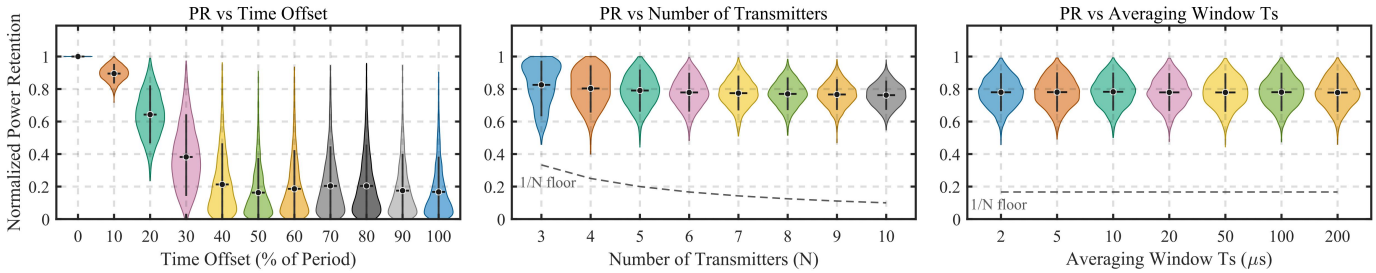

Fig. 8. Statistical analysis of the time-offset case (carrier-invariant). (a) Power Retention (PR) versus normalized time-offset half-range $\Delta\tau/T \in [0, 1]$ for $N = 6$. (b) PR versus the number of transmitters $N \in \{3, \ldots, 10\}$ at fixed $\Delta\tau/T = 15\%$. (c) PR versus averaging window $T_s \in \{2, 5, 10, 20, 50, 100, 200\}$ μs for $N = 6$ with $\Delta\tau/T = 15\%$. For each category, $M = 4000$ Monte Carlo trials draw i.i.d. per-TX delays $\tau_i \sim \mathcal{U}[-\delta T, \delta T]$ (with δ the specified half-range). Violins show empirical densities, with horizontal bars marking the means and vertical lines indicating 10–90% ranges.

5) Takeaways: First, frequency uncertainty penalizes short-time coherence with a second-order dependence on carrier, ppm spread, and window length. For small offsets ($\pi|\Delta f|T_s \ll 1$), $\mathbb{E}[\kappa_f(T_s)] \approx 1 - \frac{\pi^2}{6}\mathrm{Var}[\Delta f]\,T_s^2$ with $\mathrm{Var}[\Delta f] = 2(f_c\,10^{-6}\sigma_{\mathrm{ppm}})^2$, so doubling any one of $\{f_c, \sigma_{\mathrm{ppm}}, T_s\}$ produces a comparable PR loss. Second, carrier sensitivity is strong. For the same ppm and T_s, higher f_c implies larger $|\Delta f|$ and earlier coherence loss. Tens of ppm can remain tolerable at 915 MHz under the adopted quasi-static ppm baseline, while even single-digit ppm can already produce visible degradation at 2.4 GHz. At 60 GHz, this result should be viewed primarily as a qualitative illustration of the heightened high-frequency sensitivity within the unified framework, rather than as a quantitatively accurate prediction of practical mmWave decoherence, where dominant mechanisms stem from phase-noise spectral characteristics rather than static ppm drift. Third, enlarging the averaging window averages out beating and drives $\mathrm{PR}(T_s)$ toward $1/N$. If ppm cannot be improved, shortening T_s is the most direct lever to preserve retention. Finally, increasing N helps only while coherence is preserved. Once offsets dominate (e.g., mmWave with modest ppm and T_s), the PR distribution collapses toward the $1/N$ floor, and scaling N yields little benefit.

B. Impact of Time Offset

1) Monte Carlo Setup: Next, we examine time misalignment by setting $\Delta f = 0$ and modeling each transmitter's delay as an i.i.d. random variable. A uniform model is used as:

$$\tau_i \sim \mathcal{U}\big[-\Delta\tau, +\Delta\tau\big], \qquad \delta \triangleq \frac{\Delta\tau}{T} \in [0, 1], \tag{44}$$

and work with delays normalized by the carrier period $T = 1/f_c$, which makes the results carrier-invariant. In the unified kernel, this means $\sigma_{f,ij} = 0$ and $\sigma_{\theta,ij} = 0$, so that the coherence is controlled solely by time slip. In this case, the pairwise coherence reduces to

$$\Gamma_{ij} = \cos\left(\frac{2\pi(\tau_i - \tau_j)}{T}\right), \tag{45}$$

explicitly showing the dependence on the relative timing between the signals. For a given realization, the resulting short-time pairwise coherence is given by

$$\kappa_\tau \;=\; \frac{2}{N(N-1)} \sum_{i<j} \cos\Big(2\pi\,\frac{\tau_i - \tau_j}{T}\Big), \tag{46}$$

and with equal amplitudes the normalized power retention is

$$\mathrm{PR} \;=\; \frac{1}{N} \;+\; \Big(1 - \frac{1}{N}\Big)\kappa_\tau. \tag{47}$$

We estimate the full distribution of PR by Monte Carlo with 4,000 trials per operating point and display it using violin plots showing the mean and the 10–90% band.

2) Results: Because τ/T is dimensionless, the behavior is carrier-invariant. Therefore, we present unified results in Fig. 8. In the left subfigure (PR vs. time offset), we sweep the half-range $\delta = \Delta\tau/T$ from 0% to 100% at $N = 6$. As δ increases, pairwise phases decorrelate and PR falls from near 1 toward the incoherent floor $1/N$. In the middle (PR vs. number of transmitters), with $\delta = 15\%$ fixed we vary $N \in \{3, \ldots, 10\}$ and overlay the dashed $1/N$ baseline. For this modest dispersion, larger arrays still sit above the floor, but the margin shrinks as N grows because the floor itself drops.

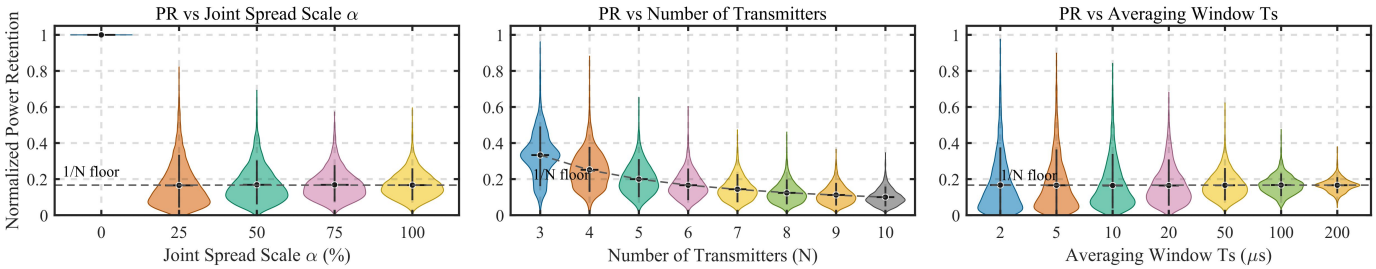

Fig. 9. All-in-one statistical impact of frequency, time, and phase offsets. Violin plots show the distribution of short-time power retention (PR) over $M = 4000$ Monte Carlo trials with quasi-static frequency offsets over the window T_s. (a) PR vs joint spread scale α that simultaneously scales $(\sigma_{\text{ppm}}, \sigma_\tau, \sigma_\theta)$; here $f_c = 915$ MHz, $N = 6$ and $T_s = 50$ μs. (b) PR vs number of transmitters N at fixed spreads ($\alpha = 1$). (c) PR vs averaging window T_s at fixed spreads and $N = 6$. Dots mark the mean; vertical bars show the 10–90% range. The dashed guide indicates the incoherent floor $1/N$.

In the right (PR vs. averaging window T_s), with $N = 6$ and $\delta = 15\%$ fixed we vary $T_s \in \{2, 5, 10, 20, 50, 100, 200\}$ μs. Since $\Delta f = 0$, there is no slow beating to average out, so PR is essentially flat versus T_s (up to Monte Carlo scatter), with the dashed line marking $1/N$.

3) Takeaways: First, carrier invariance is exact under normalization by T: the distribution of $\cos(2\pi(\tau_i - \tau_j)/T)$ depends only on the dimensionless offsets, not on f_c. Second, retention loss grows quadratically with the fractional time spread. Third, increasing N reduces the guaranteed baseline $(1/N)$ and therefore compresses the feasible range of retention. With moderate dispersion (e.g., $\delta = 15\%$) there remains headroom above $1/N$, but the margin narrows with N. Finally, unlike frequency error, increasing T_s cannot restore coherence when $\Delta f = 0$, so averaging provides no benefit.

C. Impact of Phase Offset

1) Setup and Relation to Time Offset: A static phase error at a single tone is equivalent to a normalized time offset:

$$\Delta\theta \;=\; 2\pi\,\frac{\Delta\tau}{T}, \qquad \text{with} \quad \Delta f = 0. \tag{48}$$

Hence all results in Section V-B carry over verbatim after the substitution $\Delta\tau/T \leftrightarrow \Delta\theta/(2\pi)$. To avoid redundancy, we do not introduce new figures here. For completeness, we state the phase-domain model and metric. Let each transmitter's carrier phase be i.i.d. uniform,

$$\theta_i \sim \mathcal{U}\big[-\Delta\theta,\, +\Delta\theta\big], \tag{49}$$

which is already dimensionless (carrier-invariant). In the unified kernel, this means $\sigma_{f,ij} = 0$ and $\sigma_{\tau,ij} = 0$, so that the coherence is controlled solely by phase dispersion. In this case, the pairwise coherence reduces to

$$\Gamma_{ij} \;=\; \cos\big(\theta_i - \theta_j\big). \tag{50}$$

The short-time pairwise coherence is

$$\kappa_\theta \;=\; \frac{2}{N(N-1)} \sum_{i<j} \cos\big(\theta_i - \theta_j\big), \tag{51}$$

and, for equal amplitudes, the normalized power retention is

$$\mathrm{PR} \;=\; \frac{1}{N} \;+\; \Big(1 - \frac{1}{N}\Big)\kappa_\theta. \tag{52}$$

2) Results by Mapping: Using the mapping $\Delta\tau/T \leftrightarrow \Delta\theta/(2\pi)$, the three empirical behaviors established for time offset apply identically. Increasing the half-range $\Delta\theta$ decorrelates pairwise terms and drives PR from near 1 toward the incoherent floor $1/N$. In addition, for a fixed, modest $\Delta\theta$, larger N still yields benefit above $1/N$, but the margin shrinks as N grows because the floor itself drops. Moreover, with $\Delta f = 0$, a static phase error produces a stationary envelope, so PR is essentially flat versus T_s (no slow beating to average).

3) Takeaways: First, phase dispersion is fully captured by the dimensionless spread $\Delta\theta$ and is thus carrier-invariant; all trends follow directly from the time-offset results under the mapping $\Delta\tau/T \leftrightarrow \Delta\theta/(2\pi)$. Second, for small spreads the retention loss is quadratic: with $\theta_i \sim \mathcal{U}[-\Delta\theta, \Delta\theta]$, $\mathbb{E}[\kappa_\theta] \approx 1 - \frac{2}{3}(\Delta\theta)^2$, so $\mathbb{E}[\mathrm{PR}] \approx 1 - \big(1 - \frac{1}{N}\big)\frac{2}{3}(\Delta\theta)^2$; keeping the rms phase well below one radian preserves most coherent gain. Third, increasing N lowers the guaranteed baseline $1/N$ and compresses the feasible retention band, so any uncontrolled phase spread becomes more consequential in dense charging scenarios. Fourth, unlike frequency offset, enlarging the averaging window T_s does not recover coherence for a static phase error when $\Delta f = 0$; the envelope is stationary and PR is essentially flat versus T_s. Finally, the practical knob is alignment, not averaging: calibration, phase trim, or shared phase references are the effective levers to maintain a target PR as N scales.

D. Joint Impact of Frequency, Time, and Phase

1) Monte Carlo Setup: We jointly randomize frequency, time, and phase offsets and evaluate short-time power retention via the unified pairwise coherence. For each trial and transmitter i we draw

$$\varepsilon_i \sim \mathcal{N}(0, \sigma^2_{\text{ppm}}), \quad \tau_i \sim \mathcal{N}(0, \sigma^2_\tau), \quad \theta_i \sim \mathcal{N}(0, \sigma^2_\theta),$$

and form pairwise differences $\Delta f_{ij} = f_c\, 10^{-6}(\varepsilon_i - \varepsilon_j)$, $\Delta\tau_{ij} = \tau_i - \tau_j$, $\Delta\theta_{ij} = \theta_i - \theta_j$. With a rectangular window of length T_s and equal amplitudes, the resulting normalized short-time power retention is

$$\mathrm{PR}(T_s) = \frac{1}{N} + \Big(1 - \frac{1}{N}\Big)\frac{2}{N(N-1)} \sum_{i<j} \Gamma_{ij}(T_s). \tag{53}$$

We use $M = 4000$ trials per operating point and report the full distribution of PR. To study joint severity we scale all

TABLE I
KEY SPECIFICATIONS OF A COMMERCIAL OFF-THE-SHELF POWERCAST WIRELESS POWER TRANSFER SYSTEM.

Component	Model	Frequency Range	Power (Output or Input)	Gain (dBi)	Radiation Pattern	Polarization	Return Loss
Power Transmitter	TX91501B	915 MHz (center)	3 W EIRP	8	H: 60°; V: 60°	Vertical	–
Receiving Antenna	PA-915-01	902–928 MHz	–	6.8	H: 122°; V: 68°	Vertical	<-10 dB
Receiving Antenna	DA-915-01	902–928 MHz	–	1.7	Omni-directional	Vertical	<-10 dB
Receiver Board	P2110-EVB	902–928 MHz	-12 to 10 dBm (input)	–	–	–	–

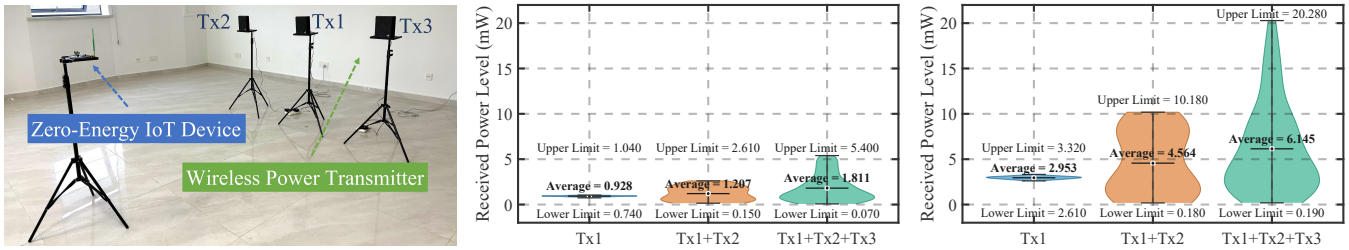

(a) Test Scenario (b) Dipole Antenna (c) Patch Antenna

Fig. 10. Experimental setup and results for concurrent WPT using Powercast wireless powering system. (a) Test layout: TX91501B transmitter(s) illuminate the measurement area while a P2110-EVB harvester serves as the receiver front-end. (b) Dipole configuration: the receiver uses the DA-915-01 (≈1.7 dBi, omni) with vertical polarization. (c) Patch configuration: the receiver uses the PA-915-01 (≈6.8 dBi, directional). The two receive antennas are evaluated in the same physical layout to contrast polarization sensitivity, beam shaping, and short-window power variability under unsynchronized multi-Tx operation.

spreads by a factor α: $(\sigma_{\mathrm{ppm}}, \sigma_\tau, \sigma_\theta) \mapsto \alpha(\sigma_{\mathrm{ppm}}, \sigma_\tau, \sigma_\theta)$. It is worth noting that if within-window frequency wander is relevant, replace the quasi-static term by the erf-based factor from Sec. III-E1. The rest of the setup is unchanged.

2) Results: Fig. 9 shows the results. For fixed (f_c, N, T_s), increasing α simultaneously enlarges ppm, time slip, and phase jitter. The PR distribution contracts from near-coherent ($\alpha \approx 0$) toward the incoherent floor $1/N$ as α grows. It is fastest when f_c or T_s are large, consistent with the quadratic budget:

$$\mathbb{E}[\bar{\Gamma}] \approx 1 - \tfrac{1}{2}\sigma^2_{\theta,ij} - \tfrac{1}{2}(2\pi f_c)^2 \sigma^2_{\tau,ij} - \tfrac{\pi^2}{6} T_s^2\, \mathbb{E}[\Delta f^2_{ij}], \quad (54)$$

so phase, time, and frequency losses add quadratically after averaging over pairs. At fixed spreads, the mean PR changes mildly with N, but the dispersion across trials shrinks rapidly ($\mathrm{Std}[\mathrm{PR}] = \Theta(N^{-1})$), concentrating performance around its mean (law of large numbers on cross terms). The dashed guide $1/N$ highlights that once offsets dominate, further increasing N mostly lowers the guaranteed baseline rather than lifting the mean. For fixed (f_c, N) and spreads, enlarging T_s averages more beat cycles from Δf_{ij} and depresses the frequency factor $\mathrm{sinc}(\pi \Delta f_{ij} T_s)$, pushing $\mathrm{PR}(T_s)$ toward $1/N$. The effect is strongest at higher f_c (larger absolute Δf_{ij}) and negligible when ppm/time/phase are already very small.

3) Takeaways: First, the joint case obeys a quadratic budget. For small dispersions the mean retention loss adds as $(\sigma_\theta)^2 + (2\pi f_c \sigma_\tau)^2 + (\pi T_s f_c \sigma_{\mathrm{ppm}})^2$, making f_c and T_s the dominant scaling factors. Second, in terms of window control, shortening T_s mitigates the frequency (sinc) term, whereas time/phase losses are T_s-independent, so T_s is a knob to trade peak capture against stability. Third, regarding scaling with N, increasing the number of transmitters concentrates PR around its mean (variance $\Theta(N^{-2})$) but cannot overcome large offsets, raising the mean requires reducing pairwise spreads (ppm, timing, or phase alignment). Finally, shared references such as a shared local oscillator, coordinated start, and phase trim help shrink pairwise dispersions and lift $\bar{\Gamma}$ without increasing transmit power.

VI. EXPERIMENTAL STUDY

In this section, we use a commercial Powercast wireless powering system [32] to experimentally illustrate the practical impact of natural asynchronicity in concurrent WPT. Quantitative experiments isolating the individual effects of frequency offset, phase offset, and time offset have been separately reported in representative prior work [15], [33]. In addition, more comprehensive experimental investigations in this hardware setting, including multidimensional studies under broader conditions, can be found in our earlier works [12], [34].

A. Testbed

The transmit side uses TX91501B beacons as continuous-wave radiators in the 915 MHz ISM band. The zero-energy IoT node consists of a P2110-EVB energy-harvesting board coupled to a WSN-EVAL-01 sensor mote, which reports per-packet received power. It should be noted that the Powercast platform reports a vendor-defined received-power/RSSI indication associated with the harvesting system, rather than a direct instantaneous-envelope-power measurement. Accordingly, the observed fluctuations are used here as qualitative evidence of beating/coherence variation. To study the effect of receiver directivity, we interchangeably mount a dipole (omnidirectional) and a patch (directional) antenna on the node. Table I summarizes the key parameters.

B. Setup and Procedure

Fig. 10a shows the geometry. Three TX91501B transmitters are arranged linearly with an inter-transmitter spacing of

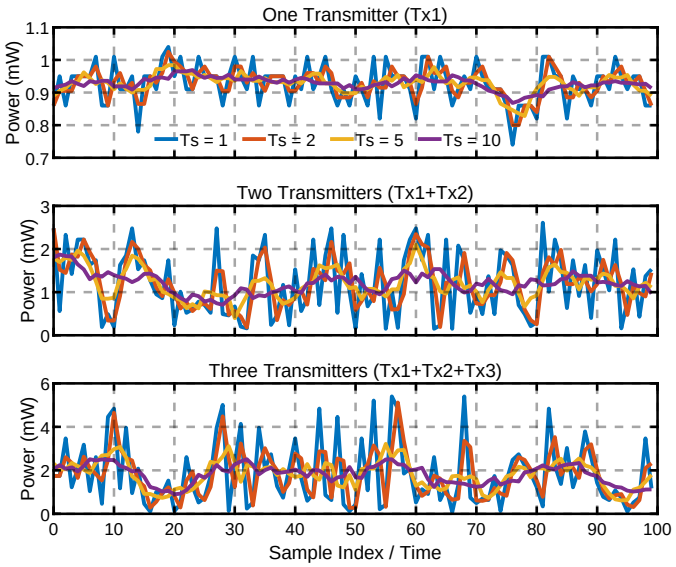

Fig. 11. Time-domain power traces with dipole antenna under different window sizes in samples. The raw power trace is processed using different observation window sizes, showing how T_s affects power fluctuations.

80 cm. The transmitter spacing of 80 cm is adopted here as a representative practical configuration [12], [34], which provides clear spatial separation between transmitters while still preserving a non-negligible overlap/interference region for observing concurrent wireless power transfer effects. The receiver is placed 2 m away on the array boresight so that all transmitters experience comparable path loss while retaining mild amplitude and phase differences due to geometry. To expose natural asynchrony, the beacons free-run without any shared timing or frequency reference. For each antenna type (dipole or patch), we collect 100 RSSI packets under three activation modes: a single-transmitter baseline (Tx1), two unsynchronized transmitters (Tx1+Tx2), and three unsynchronized transmitters (Tx1+Tx2+Tx3).

C. Impact of Transmitter Count and Receiver Antenna Type

Fig. 10b and Fig. 10c present violin plots for the dipole and patch receivers, respectively. For the dipole receiver, the single-transmitter case shows a relatively compact distribution, indicating stable received power with limited fluctuation. When additional unsynchronized transmitters are introduced, the overall received-power level tends to increase, but the distribution widens markedly, revealing much stronger variability. Under the three-transmitter condition, both the central tendency and the upper tail further increase, while low-power samples remain clearly visible. This indicates that although concurrent transmission can improve the overall power level, it also introduces frequent destructive superposition, leading to pronounced temporal fluctuations. For the patch receiver, the directional gain results in a generally higher received-power level and more prominent extremes. The single-transmitter case remains comparatively concentrated, whereas the multi-transmitter cases exhibit a clear upward shift together with substantial broadening of the distribution. As the transmitter count increases, high-power events become more evident, but the spread also grows significantly, showing that enhanced average reception is accompanied by stronger variability. Similar to the dipole case, some multi-transmitter samples still fall below the single-transmitter reference, confirming that asynchronous concurrent transmission does not guarantee uniformly improved instantaneous power.

D. Impact of Window Size

We next examine the measured power with dipole antenna under different observation window sizes in samples, i.e., $T_s = 1, 2, 5,$ and 10. For each configuration, the same measured power sequence is processed using different window sizes so that the impact of the observation timescale can be compared.

As shown in Fig. 11, the time-domain power traces are affected by the choice of T_s. When T_s is small, the processed traces retain more rapid local variations and thus reflect the short-timescale fluctuations more explicitly. As T_s increases, these short-term variations are progressively smoothed, leading to more stable and less fluctuating power traces. This effect is observed in all three transmitter configurations and is particularly visible in the concurrent transmission cases, where the measured power exhibits stronger temporal variations. Fig. 12 presents the corresponding statistical distributions by means of violin plots. For smaller T_s, the power distributions are broader, indicating stronger short-term variability. In contrast, as T_s increases, the distributions become increasingly concentrated, which shows that short-term fluctuations are gradually averaged out when a larger observation window is used. This trend is consistently observed for all three cases.

Overall, the results provide experimental support for the proposed analysis method. In particular, the experimentally observed dependence on T_s is consistent with the theoretical retention law in Eq. (18): smaller T_s preserves stronger short-time fluctuation, whereas larger T_s produces smoother traces and more concentrated distributions due to increased temporal averaging. Hence they illustrate the need for window-based multi-timescale analysis for characterizing concurrent WPT.

E. Applicability to Imbalanced Deployment Geometries

To demonstrate that the proposed model is applicable beyond idealized symmetric deployments, we conducted measurements under intentionally imbalanced geometries, as shown in Fig. 13a. In this setup, two TX91501 wireless power transmitters were placed with a total separation of 100 cm, while the P2110-EVB equipped with a dipole antenna served as the receiver. By varying the receiver position, asymmetric propagation conditions were created so as to emulate more practical deployment scenarios in which the receiver is not symmetrically located with respect to the transmitters.

Fig. 13b shows the measured time-domain power traces at 30 cm, 40 cm, and 50 cm. It can be observed that the temporal behavior of the received power varies noticeably with the receiver location. In particular, when the receiver is closer to one transmitter, the received power exhibits a different fluctuation pattern from that under more balanced conditions, reflecting the unequal contributions of the two transmitters. These results indicate that the power dynamics are geometry-dependent,

This article has been accepted for publication in IEEE Journal on Selected Areas in Communications. This is the author's version which has not been fully edited and content may change prior to final publication. Citation information: DOI 10.1109/JSAC.2026.3699841

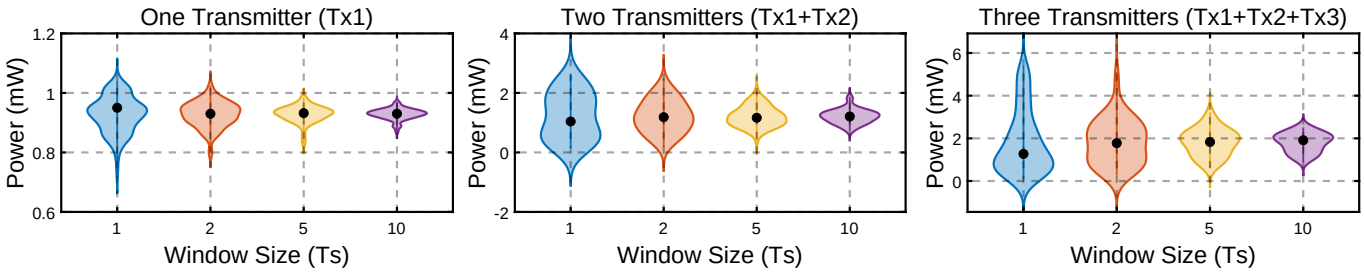

Fig. 12. Distribution of measured power with dipole antenna under different window sizes (T_s). As T_s increases, the distributions become more concentrated, indicating that short-term power fluctuations are increasingly averaged out. Note that the violin plots are obtained from kernel density estimation and therefore may slightly extend beyond the actual minimum or maximum measured values due to smoothing of the distribution tails.

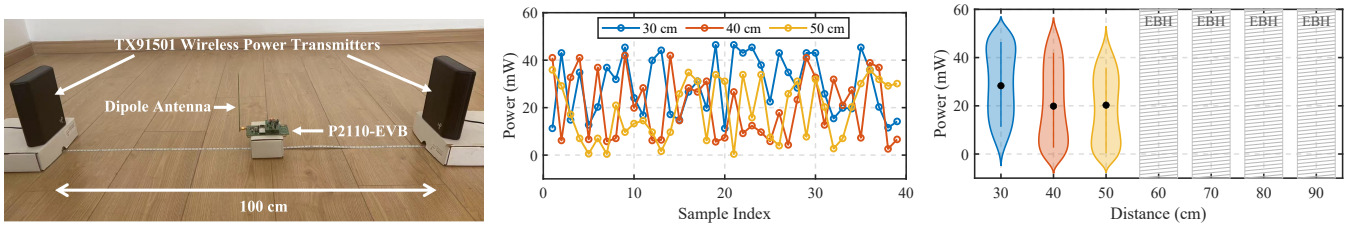

(a) Test Scenario (b) Time-Domain Power Traces (c) Statistical Distributions

Fig. 13. Experimental validation under an imbalanced deployment. (a) Measurement setup. (b) Measured time-domain power traces at receiver distances of 30 cm, 40 cm, and 50 cm. (c) Statistical distributions of the measured power from 30 cm to 90 cm. Note that the violin plots are obtained from kernel density estimation and therefore may slightly extend beyond the actual minimum or maximum measured values due to smoothing of the distribution tails.

while the proposed model remains capable of capturing the resulting variation trend. The corresponding statistical distributions from 30 cm to 90 cm are shown in Fig. 13c. In particular, at distances of 60 to 90 cm, within the overlapping coverage of both continuously operating transmitters, energy interference creates an energy black hole (EBH) [11], [35], where injected energy partially activates the hardware but fails to produce end-to-end information delivery.

VII. Conclusion

This work provides a unified quantitative treatment of asynchronous concurrent WPT tailored to sustainable 6G networks. By modeling frequency, time, and phase dispersions through a pairwise coherence kernel $\Gamma(T_s)$ and evaluating power at instantaneous, short-time, and long-time scales, we derive closed-form bounds and actionable offset budgets. The analysis reveals when and why concurrency helps versus hurts, how averaging windows trade peak capture for stability, and how carrier frequency, ppm spread, and transmitter count jointly shape retention. Monte Carlo studies yield retention distributions (not just means), enabling probabilistic guarantees under realistic ppm/jitter/phase spreads. Experiments on the commercial Powercast platform show that unsynchronized concurrency increases typical power but also inflates variance and can cause short-window underperformance.

Appendix A
General Formulation and Factorization of the Unified Coherence Kernel

A. General Formulation

Consider the pairwise short-time interaction between transmitters i and j over an averaging window T_s. Let $\Delta\Psi_{ij}(T_s)$ denote the aggregate phase perturbation induced by phase offset, timing offset, and frequency offset over that window. The corresponding pairwise coherence retention is defined as

$$\Gamma_{ij}(T_s) = \left|\mathbb{E}\left[\exp\left(j\,\Delta\Psi_{ij}(T_s)\right)\right]\right|. \tag{55}$$

This expression is exact at the level of the adopted phasor-averaging abstraction and shows that the kernel is not introduced heuristically; rather, it arises naturally as the magnitude of the averaged complex phasor under an aggregate random phase perturbation. Equivalently, let the offset vector be

$$\mathbf{x} \triangleq \left(\Delta\theta_{ij},\, \Delta\tau_{ij},\, \Delta f_{ij}\right)^T, \tag{56}$$

and let $\mathbf{u}(T_s)$ denote the deterministic scaling vector that maps these offsets into the aggregate phase perturbation over the window T_s, i.e.,

$$\Delta\Psi_{ij}(T_s) = \mathbf{u}(T_s)^T\mathbf{x}. \tag{57}$$

Then (55) can be written as

$$\Gamma_{ij}(T_s) = \left|\mathbb{E}\left[\exp\left(j\,\mathbf{u}(T_s)^T\mathbf{x}\right)\right]\right|, \tag{58}$$

which is the magnitude of the joint characteristic function of $\mathbf{x}$ evaluated at $\mathbf{u}(T_s)$. This formulation makes clear that the unified kernel is fundamentally a joint-coherence object. The multiplicative expression used in the main text is recovered under additional separability assumptions, as explained next.

B. Factorization under Independence or Separability

When the components of $\mathbf{x}$ are independent, or are approximately separable at the time scale of interest, the joint characteristic function factorizes:

$$\mathbb{E}\left[e^{j(u_1x_1+u_2x_2+u_3x_3)}\right] = \prod_{k=1}^{3}\mathbb{E}\left[e^{ju_kx_k}\right]. \tag{59}$$

Accordingly, the kernel becomes a product of marginal coherence terms. This yields the multiplicative kernel structure adopted in Eq. (14), in which phase, timing, and frequency offsets contribute distinct retention factors.

Under the Gaussian small-dispersion modeling adopted in the main text, the phase and timing factors reduce to

$$\exp\left(-\frac{\sigma_{\theta,ij}^2}{2}\right), \qquad \exp\left(-\frac{(2\pi f_c)^2\,\sigma_{\tau,ij}^2}{2}\right), \tag{60}$$

while the frequency factor is represented by $\Phi_f(\cdot, T_s)$, whose standard forms are derived in Appendix B. Therefore, under independence/separability, Eq. (14) is recovered as a tractable baseline design law.

C. Correlated-Offset Extension

If the offsets are not independent, the framework still holds, but the kernel is no longer a simple product of marginal terms. For example, if $\mathbf{x}$ is jointly Gaussian with covariance matrix $\mathbf{\Sigma}$, then the characteristic function gives

$$\Gamma_{ij}(T_s) = \exp\left(-\frac{1}{2}\mathbf{u}(T_s)^T\mathbf{\Sigma}\,\mathbf{u}(T_s)\right). \tag{61}$$

Expanding the quadratic form yields

$$\Gamma_{ij}(T_s) = \exp\left(-\frac{1}{2}\sum_k u_k^2\sigma_k^2 - \sum_{m<n} u_m u_n \Sigma_{mn}\right), \tag{62}$$

where $\sigma_k^2 = \Sigma_{kk}$ and Σ_{mn} are the off-diagonal covariance terms. The diagonal-only part corresponds to the separable kernel, whereas the off-diagonal terms capture cross-coupling corrections induced by offset correlation. Therefore, correlation among phase, timing, and frequency offsets does not invalidate the unified-kernel framework; it extends the separable kernel to a joint form with cross terms. In this paper, we adopt the separable form in Eq. (14) as a tractable and physically interpretable baseline design law, while recognizing that correlated effects may be incorporated through the joint form in (61) when correlation information is available.

D. Remark on Unknown Correlation

When correlation information is unavailable, the separable kernel in Eq. (14) may be viewed as a transparent diagonal baseline. For the jointly Gaussian case, write

$$\Sigma_{mn} = \rho_{mn}\sigma_m\sigma_n, \qquad |\rho_{mn}| \le 1. \tag{63}$$

Then (61) implies the lower bound

$$\Gamma_{ij}(T_s) \ge \exp\left(-\frac{1}{2}\sum_k u_k^2\sigma_k^2 - \sum_{m<n} |u_m u_n|\,|\rho_{mn}|\,\sigma_m\sigma_n\right). \tag{64}$$

Thus, correlation effects can be interpreted as explicit corrections around the separable baseline. When only bounds on correlation are available, it provides a conservative lower bound with respect to the assumed uncertainty set on ρ_{mn}.

APPENDIX B
DERIVATION OF THE TWO STANDARD FREQUENCY RETENTION MODELS

A. Starting Point: Windowed Cross-Term Retention

Consider the pairwise cross term between transmitters i and j in the received field superposition. Over an averaging window of duration T_s, the frequency-dependent retention factor is defined from the normalized windowed average of the complex oscillatory term:

$$\Phi_f(T_s) = \left|\frac{1}{T_s}\int_0^{T_s} e^{j2\pi\Delta f_{ij}(t)\,t}\,dt\right|, \tag{65}$$

where $\Delta f_{ij}(t)$ denotes the pairwise instantaneous frequency offset over the window. Two practically relevant cases are considered.

B. Case A: Quasi-Static Frequency Offset over T_s

When the pairwise frequency offset is approximately constant within the averaging window, i.e.,

$$\Delta f_{ij}(t) \approx \Delta f_{ij}, \qquad t \in [0, T_s], \tag{66}$$

the retention factor in (65) becomes

$$\Phi_f(\Delta f_{ij}, T_s) = \left|\frac{1}{T_s}\int_0^{T_s} e^{j2\pi\Delta f_{ij}t}\,dt\right|. \tag{67}$$

Evaluating the integral gives

$$\frac{1}{T_s}\int_0^{T_s} e^{j2\pi\Delta f_{ij}t}\,dt = \frac{e^{j2\pi\Delta f_{ij}T_s}-1}{j2\pi\Delta f_{ij}T_s}. \tag{68}$$

Using

$$e^{jx}-1 = e^{jx/2}\left(e^{jx/2}-e^{-jx/2}\right) = 2j\,e^{jx/2}\sin(x/2), \tag{69}$$

we obtain

$$\Phi_f(\Delta f_{ij}, T_s) = \left|\frac{\sin(\pi\Delta f_{ij}T_s)}{\pi\Delta f_{ij}T_s}\right| = \left|\mathrm{sinc}(\pi\Delta f_{ij}T_s)\right|. \tag{70}$$

This is the quasi-static model used in Eq. (15). It applies when the relative oscillator mismatch remains essentially constant within the harvester averaging window.

C. Case B: Within-Window Frequency Wander

We next consider the case where the pairwise frequency offset fluctuates randomly within the window due to oscillator wander, phase noise accumulation, or mobility-induced residual Doppler variation. In this case, we model the instantaneous pairwise frequency offset as a zero-mean Gaussian random variable:

$$\Delta f \sim \mathcal{N}(0, \sigma_{f,ij}^2), \tag{71}$$

where $\sigma_{f,ij}$ is the standard deviation of the instantaneous frequency offset over the window T_s.

The corresponding expected complex oscillatory term is

$$\mathbb{E}\left[e^{j2\pi\Delta f\,t}\right]. \tag{72}$$

Using the characteristic function of a zero-mean Gaussian random variable, namely

$$\mathbb{E}[e^{juX}] = e^{-\frac{1}{2}u^2\sigma^2}, \quad X \sim \mathcal{N}(0, \sigma^2), \tag{73}$$

and setting $u = 2\pi t$, we obtain

$$\mathbb{E}\left[e^{j2\pi\Delta f\, t}\right] = \exp\left(-2\pi^2\sigma_{f,ij}^2 t^2\right). \tag{74}$$

Therefore, the frequency retention factor is given by the window average of the expected coherence:

$$\Phi_f(\sigma_{f,ij}, T_s) = \frac{1}{T_s}\int_0^{T_s} \exp\left(-2\pi^2\sigma_{f,ij}^2 t^2\right)\, dt. \tag{75}$$

To evaluate the integral, define

$$a = 2\pi^2\sigma_{f,ij}^2. \tag{76}$$

Then

$$\int_0^{T_s} e^{-at^2}\, dt = \frac{\sqrt{\pi}}{2\sqrt{a}}\,\mathrm{erf}\left(\sqrt{a}\,T_s\right), \tag{77}$$

which yields

$$\Phi_f(\sigma_{f,ij}, T_s) = \frac{1}{T_s}\cdot\frac{\sqrt{\pi}}{2\sqrt{2}\pi\sigma_{f,ij}}\,\mathrm{erf}\left(\sqrt{2}\pi\sigma_{f,ij}T_s\right). \tag{78}$$

Hence,

$$\Phi_f(\sigma_{f,ij}, T_s) = \frac{\sqrt{\pi}\,\mathrm{erf}\left(\sqrt{2}\pi\sigma_{f,ij}T_s\right)}{2\sqrt{2}\pi\sigma_{f,ij}T_s}. \tag{79}$$

This is the within-window wander model used in Eq. (16).

REFERENCES

[1] N. C. Luong, T. Huynh-The *et al.*, "Advanced Learning Algorithms for Integrated Sensing and Communication (ISAC) Systems in 6G and Beyond: A Comprehensive Survey," *IEEE Communications Surveys & Tutorials*, vol. 28, pp. 2572–2611, 2026.

[2] H. Lei, X. Wu *et al.*, "3D Trajectory Design for Energy-Constrained Aerial CRNs Under Probabilistic LoS Channel," *IEEE Transactions on Cognitive Communications and Networking*, vol. 11, no. 3, pp. 1522–1534, 2025.

[3] A. Ranjha, G. Srivastava *et al.*, "Zero solarwing: A net-zero solar wind-powered uav-enabled ris system for urllc services in 6g compute first networks," *IEEE Transactions on Consumer Electronics*, vol. 71, no. 3, pp. 8141–8152, 2025.

[4] Y. Liu, D. Li *et al.*, "Rethinking Sustainable Sensing in Agricultural Internet of Things: From Power Supply Perspective," *IEEE Wireless Communications*, vol. 29, no. 4, pp. 102–109, 2022.

[5] S. Javed and M.-S. Alouini, "System Design and Parameter Optimization for Remote Coverage From NOMA-Based High-Altitude Platform Stations (HAPS)," *IEEE Transactions on Wireless Communications*, vol. 24, no. 2, pp. 1387–1400, 2025.

[6] C. Psomas, K. Ntougias *et al.*, "Wireless Information and Energy Transfer in the Era of 6G Communications," *Proceedings of the IEEE*, vol. 112, no. 7, pp. 764–804, 2024.

[7] O. López, R. K. Singh *et al.*, "Zero-Energy Devices for 6G: Technical Enablers at a Glance," *IEEE Internet of Things Magazine*, vol. 8, no. 3, pp. 14–22, 2025.

[8] Y. Liu, D. Li *et al.*, "Understanding the Impact of Environmental Conditions on Zero-Power Internet of Things: An Experimental Evaluation," *IEEE Wireless Communications*, vol. 30, no. 6, pp. 152–159, 2023.

[9] T. Liu, Y. Ma *et al.*, "Concurrent Charging With Wave Interference for Multiple Chargers," *IEEE/ACM Transactions on Networking*, vol. 32, no. 3, pp. 2525–2538, 2024.

[10] J. Xue, D. Wu *et al.*, "Charger Placement with Wave Interference," *IEEE Transactions on Mobile Computing*, vol. 24, no. 1, pp. 261–275, 2025.

[11] Y. Liu, M. Gidlund *et al.*, "Autonomous Networked Wireless Power Transfer for the Internet of Batteryless Things: Future Vision and Research Opportunities," *IEEE Wireless Communications*, vol. 32, no. 6, pp. 165–172, 2025.

[12] Y. Liu, D. Li *et al.*, "Understanding Concurrent Radiative Wireless Power Transfer in the IoT: Out of Myth, into Reality," *IEEE Wireless Communications*, vol. 31, no. 3, pp. 398–405, 2024.

[13] T. Liu, J. Gao *et al.*, "EMIT: Reflection-Based Charging Jamming Attack," *IEEE Transactions on Mobile Computing*, pp. 1–16, 2025.

[14] P. Tedeschi, S. Sciancalepore *et al.*, "Security in Energy Harvesting Networks: A Survey of Current Solutions and Research Challenges," *IEEE Communications Surveys & Tutorials*, vol. 22, no. 4, pp. 2658–2693, 2020.

[15] M. Baddeley, C. A. Boano *et al.*, "Understanding Concurrent Transmissions: The Impact of Carrier Frequency Offset and RF Interference on Physical Layer Performance," *ACM Transactions on Sensor Networks*, vol. 20, no. 1, Oct. 2023.

[16] I. Dey and N. Marchetti, "Space-Time- and Frequency- Spreading for Interference Minimization in Dense IoT," *IEEE Internet of Things Magazine*, vol. 6, no. 1, pp. 148–153, 2023.

[17] A. Mittal, Z. Xu *et al.*, "An Ultralow-Power Closed-Loop Distributed Beamforming Technique for Efficient Wireless Power Transfer," *IEEE Internet of Things Journal*, vol. 11, no. 19, pp. 31 301–31 316, 2024.

[18] Y. Alsaba, S. K. A. Rahim *et al.*, "Beamforming in Wireless Energy Harvesting Communications Systems: A Survey," *IEEE Communications Surveys & Tutorials*, vol. 20, no. 2, pp. 1329–1360, 2018.

[19] M. Ren, H. Dai *et al.*, "Understanding Wireless Charger Networks: Concepts, Current Research, and Future Directions," *IEEE Communications Surveys & Tutorials*, vol. 27, no. 4, pp. 2247–2282, 2025.

[20] M. Ren, H. Dai *et al.*, "Adaptive Charging With Beam Steering," *IEEE Transactions on Mobile Computing*, vol. 24, no. 10, pp. 11 224–11 240, 2025.

[21] Y. Zhang and C. You, "SWIPT in Mixed Near- and Far-Field Channels: Joint Beam Scheduling and Power Allocation," *IEEE Journal on Selected Areas in Communications*, vol. 42, no. 6, pp. 1583–1597, 2024.

[22] Y. Yi, G. Zhang *et al.*, "AN-Aided Secure Beamforming for ELAA-SWIPT in Mixed Near-and Far-Field," *IEEE Wireless Communications Letters*, pp. 1–1, 2025.

[23] Z. Wang, J. Hu *et al.*, "Reconfigurable Holographic Surface Assisted Wireless Energy Transfer with Non-Linear Power Amplifier: Joint Waveform and Beamforming Design," *IEEE Transactions on Wireless Communications*, pp. 1–1, 2025.

[24] F. Silva, P. Pinho *et al.*, "Multibeam Beamforming Technology in Microwave Power Transfer and Harvesting," *IEEE Journal of Microwaves*, vol. 5, no. 4, pp. 918–938, 2025.

[25] C. Lin, W. Yang *et al.*, "Near Optimal Charging Schedule for 3-D Wireless Rechargeable Sensor Networks," *IEEE Transactions on Mobile Computing*, vol. 22, no. 6, pp. 3525–3540, 2023.

[26] N. V. Bhalerao, S. K. Mothku *et al.*, "3-D AAV Deployment for Maximizing Harvested Energy in WRSNs: A Soft Actor-Critic Approach," *IEEE Internet of Things Journal*, vol. 12, no. 9, pp. 12 083–12 093, 2025.

[27] Y. Yin, D. Wu *et al.*, "SANE: Safe Charging with Wave Interference," in *IEEE INFOCOM 2025 - IEEE Conference on Computer Communications*, 2025, pp. 1–10.

[28] K. Alemdar, D. Varshney *et al.*, "RFClock: Timing, Phase and Frequency Synchronization for Distributed Wireless Networks," in *Proceedings of the 27th Annual International Conference on Mobile Computing and Networking*, ser. MobiCom '21. New York, NY, USA: Association for Computing Machinery, 2021, p. 15–27.

[29] S. He, W. Ma *et al.*, "C-Cube: Rethinking Distributed Beamforming for Concurrent Charging in Backscatter Networks," *Proc. ACM Interact. Mob. Wearable Ubiquitous Technol.*, vol. 6, no. 4, Jan. 2023.

[30] K. M. Prabhu, *Window Functions and Their Applications in Signal Processing*. Taylor & Francis, 2014.

[31] P. Pant, H. L. Dhungana *et al.*, "An Analysis of the Generalized Gaussian Integrals and Gaussian Like Integrals of Type I and II," *arXiv preprint arXiv:2508.07939*, 2025.

[32] Powercast Corporation, "Powercast: Wireless Power Technologies," https://www.powercastco.com/, 2025, accessed: 2025-09-29.

[33] K. W. Choi, A. A. Aziz *et al.*, "Distributed Wireless Power Transfer System for Internet of Things Devices," *IEEE Internet of Things Journal*, vol. 5, no. 4, pp. 2657–2671, 2018.

[34] Y. Liu, H. Wang *et al.*, "Concurrent Wireless Power Transfer in the Internet of Batteryless Things: Experiment and Modeling," *IEEE Transactions on Mobile Computing*, vol. 25, no. 3, pp. 4048–4062, 2026.

[35] Y. Liu, M. Gidlund *et al.*, "Energy Black Hole in Wireless Power Transfer: An Emerging Reliability Hazard for the Internet of Batteryless Things," *Submitted to IEEE/ACM Transactions on Networking*, 2026. (Under Review).